

Spectral boundary integral equation method for simulation of 2D and 3D slip ruptures at bi-material interfaces

Avinash Gupta*, Kunnath Ranjith

Mahindra University, École Centrale School of Engineering, Bahadurpally,
Hyderabad 500043, India

*Corresponding author

Email address: aviggupta0123@gmail.com;
avinash20pphy002@mahindrauniversity.edu.in;
ranjith.kunnath@mahindrauniversity.edu.in;

Corresponding author tel.: +91 7696944373

Abstract

This paper presents a 3D spectral numerical scheme that can accurately model planar cracks of any shape residing on an interfacial plane between two elastic solids. The cracks propagate dynamically under the action of interfacial loads and interfacial constitutive laws. The scheme is a spectral form of the boundary integral equations (BIE) that relate the displacement discontinuity fields along the interfacial plane to the stress fields at the plane. In the BIE, the displacement discontinuities are expressed as a spatio-temporal convolution of the traction components at the interface. This is in contrast with most previous studies which use a spatio-temporal convolution of the displacement discontinuities or of the displacements at the interface. Due to the continuity of tractions across the interface, the present formulation is simpler, resulting in convolution kernels that can be written in closed-form. Previous studies have relied on numerically obtained convolution kernels. The accuracy of the proposed scheme is validated with the known analytical solution of the 3D Lamb problem. Furthermore, new algorithms are developed for coupling the BIE with a slip-weakening friction law, both for homogeneous materials as well as for bi-material interfaces. This results in a widely applicable formulation for studying spontaneous rupture propagation. The algorithms are validated by comparing rupture simulation exercises to benchmark problems from Southern California Earthquake Center (SCEC). Finally, the methodology is used to simulate 3D frictional rupture propagation along a bi-material interface.

Keywords: Elasticity, Dynamic Fracture, Interface, Boundary Integral Method, Spectral

1 | Introduction

The mechanical breakdown of interfaces is an important physical phenomenon observed in both engineering and natural systems. Some domains of interest include nanotechnology,¹⁻³ micromechanical systems,⁴ tribology,⁵ composite materials^{6,7} and geophysics.^{8,9} Interfacial failure can occur in two principal forms, namely, decohesion and slipping, where materials undergo separation and slide against each other. Recent research in the field of interfacial failure has focused on developing new computational methods^{10,11} and experimental techniques^{12,13} to improve our understanding of this complex phenomenon. Despite extensive research into interface failure over many years, our understanding of the phenomenon is still incomplete. The unstable and dynamic nature of fracture and friction, coupled with their localized character, poses significant challenges for experimental investigation. Therefore, numerical simulations are essential for overcoming these challenges and providing essential insights into the physical mechanisms that govern the emergence and evolution of localized failure.

Dynamic rupture propagation at bi-material interfaces has been studied extensively in recent years. This is prompted by theoretical explorations of the role of material asymmetry in rupture dynamics. Bi-material interfaces are characterized by the coupling between slip and normal stress variations. Adams¹⁴ demonstrated that when dissimilar elastic solids sliding steadily are subjected to perturbation, a short-wavelength instability occurs when a Coulomb friction law acts at the interface. The instability is due to the destabilization of the interfacial slip wave.¹⁵ This indicates the need for modification of the Coulomb law. Specific modifications which alter the friction law at high frequencies were suggested by studies Ranjith and Rice¹⁶ and Rice et al.¹⁷ Adams¹⁸ also obtained a bi-material slip pulse solution which propagates with the slip wave speed. Additionally, Ranjith¹⁹ showed a new instability of long-wavelength interfacial Love²⁰ wave and

Stoneley²¹ wave at a bi-material interface. These findings have spurred numerous numerical investigations aimed at understanding dynamic ruptures at bi-material interfaces.

To simulate dynamic slip rupture at interfaces, numerical studies have employed various schemes, such as the finite difference method^{22,23} and the finite element method.²⁴⁻²⁶ Among proposed numerical methods, the boundary integral equation (BIE) method^{27,28} has been found to be a highly effective tool for studying dynamic crack and rupture propagation. It has been shown to accurately capture the singularities of crack-tips and wave propagation effects. It is capable of addressing problems that are spatially and temporally multi-scale. This method directly relates the field quantities at the fracture plane, i.e., the stress fields and the corresponding displacement discontinuities, and provides an accurate and efficient way to investigate both stationary planar cracks and fast-spreading cracks. This approach is numerically efficient since it only evaluates field values on the fracture plane, rather than computing them in the entire domain (i.e., an overall reduction in dimension by one) as required by conventional computational methods such as finite element and finite difference methods. This can lead to significant reductions in computation time and memory usage. In the literature, two alternative forms of the boundary integral equations have been proposed. In the first approach, the tractions (i.e., the stresses acting on the interface) are expressed as a spatio-temporal convolution of the displacement discontinuities at the interface plane, as proposed by Budiansky and Rice.²⁹ In the second approach, the displacement discontinuities are formulated as a spatio-temporal convolution of the tractions at the interface plane, as proposed by Kostrov.³⁰

A spectral method based on the Budiansky-Rice²⁹ formulation was introduced by Geubelle and Rice.³¹ The field quantities, i.e., the stress fields and displacement discontinuities at the fracture plane are expanded in a finite Fourier series. This approach replaces the spatial

convolution with multiplication in the spectral domain, leading to improved computational efficiency. However, the method produces hypersingular terms in the convolution kernel, which are dealt with by explicitly removing the radiation damping response. The formulation is well-suited for parallel computing because of its spectral nature. Although the spectral boundary integral (SBI) method is restricted to studying fracture propagation in a plane, it can handle complex problems which are less amenable to study by other methods. For example, the SBI technique has been utilized to simulate earthquake cycles, which are computationally intensive and challenging to analyze using conventional methods like finite difference or finite element methods. The SBI method was extended to interfaces between dissimilar materials by Geubelle and Breitenfeld³² and Breitenfeld and Geubelle³³ in 2D and 3D. They introduced two formulations for bi-material problems: an "independent" formulation and a "combined" formulation. In the "independent" formulation, the BIE are developed independently for the two solids forming the interface and solved separately in conjunction with the constitutive laws at the interface. In contrast, the "combined" formulation directly solves the displacement discontinuities at the interface together with the constitutive laws at the interface, resulting in higher computational efficiency. They observed that the "combined" formulation was less numerically stable than the "independent" formulation. Recently, Ranjith^{34,35} proposed an alternative spectral form of BIE for 2D in-plane and antiplane bi-material problems based on Kostrov's approach.³⁰ This approach uses elastodynamic convolutions of the traction components of stress at the interface. In the present study, a new spectral formulation for 3D elastodynamic problems for fracture on planar interfaces between dissimilar elastic half-spaces is proposed based on Ranjith's 2D formulation.^{34,35} The proposed SBI method and frictional constitutive law are used numerically to study rupture propagation at a bi-material interface.

Figure 1 illustrates the geometric aspects of the interfacial fracture problem. A crack of arbitrary geometry is present at the interface between separating two semi-infinite elastic half spaces. A Cartesian coordinate system, with coordinates, $x_i, (i = 1,2,3)$ and time t is used to describe the problem. The fracture plane is situated at $x_2 = 0$, and x_1 and x_3 are the coordinates in the fracture plane. The elastodynamic fields are present in the half-spaces $x_2 > 0$ and $x_2 < 0$. Let $u_i(x_1, x_2, x_3, t), i = 1,2,3$ and $\sigma_{ij}(x_1, x_2, x_3, t), i, j = 1,2,3$ represent the displacement components and the stress components, respectively. Thus, the traction components of stress on the fracture plane and displacement components on the fracture plane are

$$\tau_i(x_1, x_3, t) = \sigma_{i2}(x_1, x_2 = 0^\pm, x_3, t) \quad (1)$$

$$u_i^\pm(x_1, x_3, t) = u_i(x_1, x_2 = 0^\pm, x_3, t),$$

respectively. The superscripts “ \pm ” refer to field quantities correspond to the top and lower half-space, respectively. Similar notation is used for material properties in the adjoining half-spaces. The displacement discontinuities on the fracture plane are thus

$$\delta_i(x_1, x_3, t) = u_i^+(x_1, x_3, t) - u_i^-(x_1, x_3, t). \quad (2)$$

The BIE has been extensively employed in the literature to investigate crack propagation or rupture propagation at a planar interface between elastic half-spaces. The key benefit of this method over conventional methods such as finite element or finite difference methods is that it does not require the need to model wave propagation throughout the entire domain. Instead, it only uses the displacement fields and tractions components along the planar interface. This results in improved numerical efficiency in comparison to conventional finite element or finite difference methods. For an interface between two identical solids, the BIE proposed by Budiansky and Rice²⁹ are written in the form:³⁶

$$\tau_i(x_1, x_3, t) = \tau_i^0(x_1, x_3, t) - V_{ij} \dot{\delta}_i(x_1, x_3, t) + f_i(x_1, x_3, t), \quad (3)$$

where $[V_{ij}]$ is a diagonal matrix with $V_{11} = V_{33} = \frac{\mu}{2c_s}$ and $V_{22} = \frac{\lambda+2\mu}{2c_d}$. The functionals f_i are linear and involve convolutions of the displacement discontinuities at the fracture plane in space-time, while τ_i^0 represents the externally applied loads far from the fracture. Furthermore, λ and μ are the Lamé parameters of the two solids. The shear and dilatational wave speeds of the solids are given by $c_s = \sqrt{\mu/\rho}$ and $c_d = \sqrt{(\lambda + 2\mu)/\rho}$, respectively, where ρ is the density of the solid.

To prevent singularities in the convolution kernels, the radiation damping term is explicitly separated. It is the second term on the right-hand side of Equation (3). The spectral form of Equation (3) was first presented by Geubelle and Rice,³¹ in which the tractions and displacement discontinuities are expressed in the following form:

$$\begin{aligned} \tau_j(x_1, x_3, t) &= \sum_k \sum_m T_j(t; k, m) \exp(ikx_1 + imx_3) \\ \delta_j(x_1, x_3, t) &= \sum_k \sum_m D_j(t; k, m) \exp(ikx_1 + imx_3) \\ f_j(x_1, x_3, t) &= \sum_k \sum_m F_j(t; k, m) \exp(ikx_1 + imx_3), \end{aligned} \quad (4)$$

where T_j , D_j and F_j are the spectral amplitudes of the tractions, displacement discontinuities and the functional, respectively, while k and m are the wavenumbers. The convolution kernels in the spectral domain, $F_j(t; k, m)$, were obtained by Geubelle and Rice.³¹

Later, Geubelle and Breitenfeld³² and Breitenfeld and Geubelle³³ extended this spectral formulation to the bi-material interface. They developed a bi-material spectral scheme for the 2D

antiplane and 2D in-plane problems, followed by a scheme for the fully 3D fracture problems. They introduced two approaches, referred to as the “independent” formulation and the “combined” formulation. The “independent” involves using the BIE for each half-space separately before imposing the interfacial constitutive law. The alternative “combined” formulation involves formulating the BIE directly for the displacement discontinuities. It was numerically less stable and consequently not used. In the “independent”, the elastodynamic convolutions are performed over the history of displacement components for the two half-spaces. For an interface between dissimilar solids, they wrote the BIE at the interface for each half-space in the form:

$$\tau_i(x_1, x_3, t) = \tau_i^0(x_1, x_3, t) \mp V_{ij} \dot{u}_i^\pm(x_1, x_3, t) + f_i^\pm(x_1, x_3, t), \quad (5)$$

where $[V_{ij}]$ is a diagonal matrix with $V_{11} = V_{33} = \frac{\mu^\pm}{c_s^\pm}$ and $V_{22} = \frac{\lambda^\pm + 2\mu^\pm}{c_d^\pm}$ and f_i are linear functionals that involve spatio-temporal convolutions of the displacement fields at the fracture plane.

Recently, Ranjith^{34,35} proposed an alternative spectral form based on Kostrov's BIE³⁰ for 2D bi-material in-plane and antiplane strain deformation. In their approach, the convolutions in space-time are performed over the tractions at the interface instead of the displacement fields or displacement discontinuities. Due to traction continuity at the interface, integral equations for the combined elastodynamic responses of the half-spaces in terms of the displacement discontinuities are obtained. For an interface between dissimilar materials, Kostrov's BIE³⁰ equations can be written as

$$A_{ij}(\tau_i(x_1, x_3, t) - \tau_i^0(x_1, x_3, t)) + \dot{\delta}_i(x_1, x_3, t) = f_i(x_1, x_3, t), \quad (6)$$

where $[A_{ij}]$ is a diagonal matrix with $A_{11} = A_{33} = \frac{c_s^+}{\mu^+} + \frac{c_s^-}{\mu^-}$, $A_{22} = \frac{c_d^+}{\lambda^+ + 2\mu^+} + \frac{c_d^-}{\lambda^- + 2\mu^-}$. The functionals f_i involve spatio-temporal convolutions of the tractions at the fracture plane. The rates of the displacement discontinuities, $\dot{\delta}_i(x_1, x_3, t)$, depend on all three components of the tractions due to material dissimilarity across the interface. Since the tractions are continuous at the interface, obtaining a relation between displacement discontinuities or displacements and tractions is easier compared to the approach proposed by Geubelle and Breitenfeld³² and Breitenfeld and Geubelle.³³ This study presents a 3D spectral formulation by combining bi-material in-plane and antiplane shear solutions described by Ranjith.^{34,35} The formulation is then coupled with a constitutive law for the interface to simulate dynamic rupture propagation.

The paper is structured as follows: The 3D spectral formulation for a bi-material interface is derived in Section 2. Section 3 describes the simulations performed to validate the proposed method with the analytical solutions of the 3D Lamb problem for half-spaces and for bi-material interfaces. In Sections 4 and 5, algorithms for the integration of a friction law with the BIE are discussed for studying rupture propagation at the bi-material interface in 2D and 3D, respectively. The algorithms are validated against benchmark problems from the Southern California Earthquake Center (SCEC, <https://strike.scec.org/cvws/>). The methodology is then used to simulate 3D frictional rupture propagation along a bi-material interface. In Section 6, a comparative study between the proposed and prior schemes is discussed. The results are finally summarized in Section 7.

2 | Methodology

2.1 | 2D spectral formulation

First, we summarize the results of the 2D formulation. Consider a state of plane strain so that the displacements and stress fields depend only on x_1 and x_2 . Let $T_j(t; q)$ and $U_j(t; q)$ denote the spectral amplitudes of the q th-mode of the traction stresses and displacements acting along the interface, respectively, as in

$$\tau_j(x_1, t) = T_j(t; q) \exp(iqx_1) \quad (7)$$

$$u_j^\pm(x_1, t) = U_j^\pm(t; q) \exp(iqx_1).$$

Here, $j = 1, 2$ correspond to the in-plane problem $j = 3$ corresponds to the antiplane problem. The inplane and antiplane problems have been studied by Ranjith³⁴ and Ranjith,³⁵ respectively. We focus now on the 3D case by combining those solutions. Starting from Equation (11) of Ranjith³⁴ and Equation (10) of Ranjith,³⁵

$$\begin{aligned} \hat{U}_1^\pm(p; q) = & \mp \frac{1}{\mu^\pm |q|} \frac{\alpha_s^\pm (1 - \alpha_s^{\pm 2})}{4\alpha_s^\pm \alpha_d^\pm - (1 + \alpha_s^{\pm 2})^2} \hat{T}_1(p; q) \\ & - \frac{1}{iq\mu^\pm} \frac{2\alpha_s^\pm \alpha_d^\pm - (1 + \alpha_s^{\pm 2})^2}{4\alpha_s^\pm \alpha_d^\pm - (1 + \alpha_s^{\pm 2})^2} \hat{T}_2(p; q) \end{aligned} \quad (8)$$

$$\begin{aligned} \hat{U}_2^\pm(p; q) = & \frac{1}{iq\mu^\pm} \frac{2\alpha_s^\pm \alpha_d^\pm - (1 + \alpha_s^{\pm 2})^2}{4\alpha_s^\pm \alpha_d^\pm - (1 + \alpha_s^{\pm 2})^2} \hat{T}_1(p; q) \\ & \mp \frac{1}{\mu^\pm |q|} \frac{\alpha_d^\pm (1 - \alpha_s^{\pm 2})}{4\alpha_s^\pm \alpha_d^\pm - (1 + \alpha_s^{\pm 2})^2} \hat{T}_2(p; q) \end{aligned}$$

$$\hat{U}_3^\pm(p; q) = \mp \frac{1}{\mu^\pm |q| \alpha_s^\pm} \hat{T}_3(p; q),$$

where $\hat{f}(p)$ denotes the Laplace transform of $f(t)$, defined by $\hat{f}(p) = \int_0^\infty f(t)e^{-pt}dt$, and

$$\alpha_s^\pm = \sqrt{1 + p^2/q^2 c_s^{\pm 2}}, \quad \alpha_d^\pm = \sqrt{1 + p^2/q^2 c_d^{\pm 2}}. \quad (9)$$

Defining $\delta_j(x_1, t) = (U_j^+(t; q) - U_j^-(t; q)) \exp(iqx_1) \equiv D_j(t; q) \exp(iqx_1)$, and rewriting

Equation (8) in term of D_j and T_j and extracting the instantaneous response, gives

$$\begin{aligned} & \left\{ \begin{array}{l} \frac{c_s^+}{\mu^+} \eta \hat{T}_1(p; q) \\ \frac{c_s^+}{\mu^+} \xi \hat{T}_2(p; q) \\ \frac{c_s^+}{\mu^+} \eta \hat{T}_3(p; q) \end{array} \right\} + p \left\{ \begin{array}{l} \hat{D}_1(p; q) \\ \hat{D}_2(p; q) \\ \hat{D}_3(p; q) \end{array} \right\} \\ &= \begin{bmatrix} \hat{M}_{11}^+ + \hat{M}_{11}^- & \hat{M}_{12}^+ - \hat{M}_{12}^- & 0 \\ \hat{M}_{21}^+ - \hat{M}_{21}^- & \hat{M}_{22}^+ + \hat{M}_{22}^- & 0 \\ 0 & 0 & \hat{M}_{33}^+ + \hat{M}_{33}^- \end{bmatrix} \left\{ \begin{array}{l} \hat{T}_1(p; q) \\ \hat{T}_2(p; q) \\ \hat{T}_3(p; q) \end{array} \right\}, \end{aligned} \quad (10)$$

where the associated Laplace-Fourier transfer functions are given by

$$\begin{aligned} \hat{M}_{11}^\pm(p; q) &= \frac{c_s^\pm}{\mu^\pm} - \frac{p}{\mu^\pm |q|} \frac{\alpha_s^\pm (1 - \alpha_s^{\pm 2})}{4\alpha_s^\pm \alpha_d^\pm - (1 + \alpha_s^{\pm 2})^2} \\ \hat{M}_{22}^\pm(p; q) &= \frac{c_d^\pm}{\lambda^\pm + 2\mu^\pm} - \frac{p}{\mu^\pm |q|} \frac{\alpha_d^\pm (1 - \alpha_s^{\pm 2})}{4\alpha_s^\pm \alpha_d^\pm - (1 + \alpha_s^{\pm 2})^2} \\ \hat{M}_{33}^\pm(p; q) &= \frac{c_s^\pm}{\mu^\pm} - \frac{p}{\mu^\pm |q| \alpha_s^\pm} \end{aligned} \quad (11)$$

$$\widehat{M}_{12}^{\pm}(p; q) = -\frac{p}{iq\mu^{\pm}} \frac{2\alpha_s^{\pm}\alpha_d^{\pm} - (1 + \alpha_s^{\pm 2})^2}{4\alpha_s^{\pm}\alpha_d^{\pm} - (1 + \alpha_s^{\pm 2})^2} = -\widehat{M}_{21}^{\pm}(p; q),$$

with $\eta = \left(1 + \frac{c_s^- \mu^+}{c_s^+ \mu^-}\right)$ and $\xi = \left(\frac{c_s^+}{c_d^+} + \frac{c_s^- \mu^+}{c_s^+ \mu^-} \frac{c_s^-}{c_d^-}\right)$. Reverting back to the space-time domain, the above BIE relations (Equation (10)) can be written in the form

$$\begin{pmatrix} \frac{c_s^+}{\mu^+} \eta T_1(t; q) + \frac{\partial D_1(t; q)}{\partial t} \\ \frac{c_s^+}{\mu^+} \xi T_2(t; q) + \frac{\partial D_2(t; q)}{\partial t} \\ \frac{c_s^+}{\mu^+} \eta T_3(t; q) + \frac{\partial D_3(t; q)}{\partial t} \end{pmatrix} = \begin{pmatrix} F_1(t; q) \\ F_2(t; q) \\ F_3(t; q) \end{pmatrix} \quad (12)$$

where convolution terms are given by

$$\begin{pmatrix} F_1(t; q) \\ F_2(t; q) \\ F_3(t; q) \end{pmatrix} = \int_0^t \begin{bmatrix} M_{11}^+(t'; q) + M_{11}^-(t'; q) & M_{12}^+(t'; q) - M_{12}^-(t'; q) & 0 \\ M_{21}^+(t'; q) - M_{21}^-(t'; q) & M_{22}^+(t'; q) + M_{22}^-(t'; q) & 0 \\ 0 & 0 & M_{33}^+(t'; q) + M_{33}^-(t'; q) \end{bmatrix} \begin{pmatrix} T_1(t - t'; q) \\ T_2(t - t'; q) \\ T_3(t - t'; q) \end{pmatrix} dt'.$$

The convolution terms mentioned above involve in-plane (mode I and mode II) convolution kernels $M_{11}(k, t)$, $M_{22}(k, t)$ and $M_{12}(k, t)$ as well as antiplane (mode III) convolution kernel $M_{33}(k, t)$. The closed form expressions for these kernels have been provided by Ranjith³⁴ and Ranjith,³⁵ respectively and are given in Appendix A. In the space-time domain, the BIE relations take the form

$$\begin{aligned}
\frac{c_s^+}{\mu^+} \eta(\tau_1(x_1, t) - \tau_1^0(x_1, t)) + \dot{\delta}_1(x_1, t) &= f_1(x_1, t) \\
\frac{c_s^+}{\mu^+} \xi(\tau_2(x_1, t) - \tau_2^0(x_1, t)) + \dot{\delta}_2(x_1, t) &= f_2(x_1, t) \\
\frac{c_s^+}{\mu^+} \eta(\tau_3(x_1, t) - \tau_3^0(x_1, t)) + \dot{\delta}_3(x_1, t) &= f_3(x_1, t)
\end{aligned} \tag{13}$$

which is the 2D form of Equation (6).

2.2 | 3D spectral formulation

We extend the two-dimensional results presented in the Section 2.1 to three-dimensional case. A harmonic variation of the displacements, stresses, displacement discontinuities and elastodynamic functional on the fracture plane with respect to the x_1 - and x_3 -coordinates are considered:

$$\begin{aligned}
u_j^\pm(x_1, x_3, t) &= U_j^\pm(t; k, m) e^{(ikx_1 + imx_3)} \\
[\tau_j(x_1, x_3, t), \delta_j(x_1, x_3, t), f_j(x_1, x_3, t)] \\
&= [T_j(t; k, m), D_j(t; k, m), F_j(t; k, m)] e^{(ikx_1 + imx_3)}.
\end{aligned} \tag{14}$$

The wave number q , which was used in the two-dimensional formulation, has been replaced by a two-dimensional wave vector $\mathbf{q} = (k, m)$ in the three-dimensional case. This wave vector spans the fracture plane and its magnitude is defined by $q = \sqrt{k^2 + m^2}$. The displacement field \mathbf{U} and stress field \mathbf{T} for a general three-dimensional scenario can be obtained by performing an in-plane rotation about the x_2 -axis of the previously derived components \mathbf{U}' and \mathbf{T}' in the 2D formulation.

This results in displacement and stress fields that can be expressed as follows:

$$\{U'\} = [R]\{U\} \quad \text{and} \quad \{T'\} = [R]\{T\}, \quad (15)$$

where,

$$[R] = \frac{1}{|q|} \begin{bmatrix} k & 0 & m \\ 0 & 1 & 0 \\ -m & 0 & k \end{bmatrix} \quad \text{and} \quad |q| = \sqrt{k^2 + m^2}.$$

Equation (10) can be written in the following form by introducing Equation (15)

$$\begin{aligned} [A][R] \begin{Bmatrix} \hat{T}_1(p; k, m) \\ \hat{T}_2(p; k, m) \\ \hat{T}_3(p; k, m) \end{Bmatrix} + p[R] \begin{Bmatrix} \hat{D}_1(p; k, m) \\ \hat{D}_2(p; k, m) \\ \hat{D}_3(p; k, m) \end{Bmatrix} \\ = \begin{bmatrix} \hat{M}_{11}^+ + \hat{M}_{11}^- & \hat{M}_{12}^+ - \hat{M}_{12}^- & 0 \\ \hat{M}_{21}^+ - \hat{M}_{21}^- & \hat{M}_{22}^+ + \hat{M}_{22}^- & 0 \\ 0 & 0 & \hat{M}_{33}^+ + \hat{M}_{33}^- \end{bmatrix} [R] \begin{Bmatrix} \hat{T}_1(p; k, m) \\ \hat{T}_2(p; k, m) \\ \hat{T}_3(p; k, m) \end{Bmatrix}, \end{aligned} \quad (16)$$

where coefficient matrix $[A]$ is

$$[A] = \begin{bmatrix} \frac{c_s^+}{\mu^+} \eta & 0 & 0 \\ 0 & \frac{c_s^+}{\mu^+} \xi & 0 \\ 0 & 0 & \frac{c_s^+}{\mu^+} \eta \end{bmatrix}.$$

Rewriting Equation (16) in the following form,

$$[A] \begin{Bmatrix} \hat{T}_1(p; k, m) \\ \hat{T}_2(p; k, m) \\ \hat{T}_3(p; k, m) \end{Bmatrix} + p \begin{Bmatrix} \hat{D}_1(p; k, m) \\ \hat{D}_2(p; k, m) \\ \hat{D}_3(p; k, m) \end{Bmatrix} = \begin{bmatrix} \hat{C}_{11} & \hat{C}_{12} & \hat{C}_{13} \\ \hat{C}_{21} & \hat{C}_{22} & \hat{C}_{23} \\ \hat{C}_{31} & \hat{C}_{32} & \hat{C}_{33} \end{bmatrix} \begin{Bmatrix} \hat{T}_1(p; k, m) \\ \hat{T}_2(p; k, m) \\ \hat{T}_3(p; k, m) \end{Bmatrix}, \quad (17)$$

where the associated Laplace-Fourier transfer functions are given by

$$\begin{aligned}
\hat{C}_{11}(p; q) &= \frac{1}{q^2} [k^2(\hat{M}_{11}^+ + \hat{M}_{11}^-) + m^2(\hat{M}_{33}^+ + \hat{M}_{33}^-)] \\
\hat{C}_{22}(p; q) &= \hat{M}_{22}^+ + \hat{M}_{22}^- \\
\hat{C}_{33}(p; q) &= \frac{1}{q^2} [m^2(\hat{M}_{11}^+ + \hat{M}_{11}^-) + k^2(\hat{M}_{33}^+ + \hat{M}_{33}^-)] \\
\hat{C}_{12}(p; q) &= \frac{k}{m} \hat{C}_{32}(p; q) = -\frac{k}{m} \hat{C}_{23}(p; q) = -\hat{C}_{21}(p; q) = \frac{k}{q} [\hat{M}_{12}^+ - \hat{M}_{12}^-] \\
\hat{C}_{13}(p; q) &= \hat{C}_{31}(p; q) = \frac{km}{q^2} [(\hat{M}_{11}^+ + \hat{M}_{11}^-) - (\hat{M}_{33}^+ + \hat{M}_{33}^-)]
\end{aligned} \tag{18}$$

Thus, the BIE relations (Equation (17)) in the spectral domain can be written in the form:

$$\begin{pmatrix} \frac{c_s^+}{\mu^+} \eta T_1(t; k, m) + \frac{\partial D_1(t; k, m)}{\partial t} \\ \frac{c_s^+}{\mu^+} \xi T_2(t; k, m) + \frac{\partial D_2(t; k, m)}{\partial t} \\ \frac{c_s^+}{\mu^+} \eta T_3(t; k, m) + \frac{\partial D_3(t; k, m)}{\partial t} \end{pmatrix} = \begin{pmatrix} F_1(t; k, m) \\ F_2(t; k, m) \\ F_3(t; k, m) \end{pmatrix}, \tag{19}$$

where convolution terms are given by

$$\begin{pmatrix} F_1(t; k, m) \\ F_2(t; k, m) \\ F_3(t; k, m) \end{pmatrix} = \int_0^t \begin{bmatrix} C_{11}(t'; q) & C_{12}(t'; q) & C_{13}(t'; q) \\ C_{21}(t'; q) & C_{22}(t'; q) & C_{23}(t'; q) \\ C_{31}(t'; q) & C_{32}(t'; q) & C_{33}(t'; q) \end{bmatrix} \begin{pmatrix} T_1(t - t'; k, m) \\ T_2(t - t'; k, m) \\ T_3(t - t'; k, m) \end{pmatrix} dt'.$$

In the above equation, we have five independent convolution kernels which can be expressed as

$$\begin{aligned}
C_{11}(t; q) &= \frac{1}{q^2} [k^2(M_{11}^+ + M_{11}^-) + m^2(M_{33}^+ + M_{33}^-)] \\
C_{22}(t; q) &= M_{22}^+ + M_{22}^-
\end{aligned}$$

$$C_{33}(t; q) = \frac{1}{q^2} [m^2(M_{11}^+ + M_{11}^-) + k^2(M_{33}^+ + M_{33}^-)] \quad (20)$$

$$C_{12}(t; q) = \frac{k}{m} C_{32}(t; q) = -\frac{k}{m} C_{23}(t; q) = -C_{21}(t; q) = \frac{k}{q} [M_{12}^+ - M_{12}^-]$$

$$C_{13}(t; q) = C_{31}(t; q) = \frac{km}{q^2} [(M_{11}^+ + M_{11}^-) - (M_{33}^+ + M_{33}^-)]$$

Note that all above convolution kernels $C_{ij}(t; q)$ can be expressed in closed form in terms of obtained in-plane and antiplane kernels in the previous section. The numerical implementation of the elastodynamic traction-based formulations and the general structure of the algorithm is discussed in the Section 4, followed by a discussion of the accuracy of the numerical scheme through comparison with simple analytic solutions.

3 | Validation of the scheme

To implement the 3D spectral formulation (Equation (18)) numerically, the field quantities τ_j, δ_j and f_j are expressed as a double Fourier series. The periodicity of the domain is taken as X and Z in the x_1 - and x_3 - directions, respectively. Thus,

$$\begin{Bmatrix} \tau_j(x_1, x_3, t) \\ \delta_j(x_1, x_3, t) \\ f_j(x_1, x_3, t) \end{Bmatrix} = \sum_{k=-K/2}^{K/2} \sum_{m=-M/2}^{M/2} \begin{Bmatrix} T_j(t; k, m) \\ D_j(t; k, m) \\ F_j(t; k, m) \end{Bmatrix} \exp\left(2\pi i \left(\frac{kx_1}{X} + \frac{mx_3}{Z}\right)\right), \quad (21)$$

where, each $F_j(t; k, m)$ is linked to the corresponding $T_j(t; k, m)$ by Equation (19). The Fast Fourier Transform (FFT) is used to transition between the spatial and spectral domains. The FFT algorithm uses K sampling points in the x_1 direction and M sampling points in the x_3 direction. The spatial grid sizes thus are $\Delta x_1 = X/K$ and $\Delta x_3 = Z/M$. K and M are chosen to be even and a

power of two, to facilitate the FFT algorithm for efficient conversion between spatial and spectral distributions. The convolution terms are computed in the spectral domain using Equation (19), and then converted back into the spatial domain using inverse FFT. This conversion requires a time-integration scheme to determine how the slip fields (i.e., displacement discontinuities) evolve over time based on the slip rate values calculated at discrete time intervals. A simple explicit scheme is employed here,

$$\delta_i(x_1, x_3, t) = \delta_i(x_1, x_3, t - \Delta t) + \dot{\delta}_i(x_1, x_3, t - \Delta t)\Delta t. \quad (22)$$

The size of the time step, Δt , is determined by taking it as a fraction of the time taken by the fastest shear wave to travel the smallest grid size,

$$\Delta t = \beta \frac{\min(\Delta x_1, \Delta x_3)}{\max(c_s^+, c_s^-)}, \quad (23)$$

where β is the Courant parameter. The importance of the user-defined parameter β for the numerical scheme's stability and accuracy is discussed further in this section. Finally, the algorithm is completed by incorporating a cohesive model that relates the material shear strength to the general shear displacement using a general relation,

$$\tau_{str} = -\tau_2 f(\delta_s), \quad (24)$$

where τ_{str} represents the frictional shear strength of the interface, and δ_s represents the shear displacement discontinuities over fracture plane and is defined by

$$\delta_s = \sqrt{\delta_1^2 + \delta_3^2}. \quad (25)$$

In the remainder of this paper, a slip-weakening friction model is used at the interface, given by

$$f_{str}(\delta_s) = \begin{cases} f_s - (f_s - f_d) \frac{\delta_s}{\delta_c}, & \delta_s < \delta_c \\ f_d, & \delta_s \geq \delta_c \end{cases} \quad (26)$$

where f_s and f_d are the static and dynamic frictional coefficients, respectively, and δ_c is the critical slip needed to achieve dynamic frictional strength. In this paper, the static and dynamic frictional coefficient value are taken as $f_s = 0.677$ and $f_d = 0.525$, respectively, and δ_c is set to 0.40. This completes the general description of the proposed algorithm. The validation and stability of the bi-material implementation of the spectral scheme will be further evaluated in this section.

3.1 | 3D Lamb's Problem

The proposed spectral scheme here is validated and the optimal value of the Courant parameter β is investigated using the case of a step line load applied on an elastic half space.

Two separate cases are considered: Case A and Case B, where a step normal or tangential line load, respectively, is applied at the midpoint of the free surface (see Figure 2). The accuracy of the numerical scheme is evaluated by comparing the numerical displacement at a point located at a distance $r = \sqrt{x_1^2 + x_3^2}$ from the point of application of the load with the analytical solution provided by Kausel.³⁷

As mentioned, a step normal or tangential line load is applied at $t = 0$ at the center of the free surface of size $X * X$. The domain is discretized into 512 by 512 spatial points, so that $\Delta x_1 = \Delta x_3 = X/512$. The Courant parameter is $\beta = c_s * \Delta t / \Delta x_1$. The value of β is to be chosen so that an accurate and stable numerical solution is obtained. Poisson's ratio is taken to be 0.25. The observation point is located $X/8$ grid spacings along both x_1 and x_3 from the point of application

of the step line load. The use of superscripts + and - in the field quantities and material properties will not be necessary in this section, as only a single half-space is being considered.

In Case A, a step line load is applied normal to the free surface, given by

$$\tau_2^0(x_1, x_3, t) = P\delta(x_1)\delta(x_3)H(t) \quad (27)$$

$$\tau_1^0 = \tau_3^0 = 0,$$

where P is the load, and $H(t)$ is the Heaviside unit step function. The free surface conditions dictate that $\tau_1 = \tau_2 = \tau_3 = 0$. By substituting these values into Equation (16), the elastodynamic equations in the spectral domain can be obtained as

$$\begin{aligned} p\hat{U}_1 &= \frac{k}{q}\hat{M}_{12}\hat{T}_2 \\ \frac{c_s}{\mu}\frac{c_s}{c_d}\hat{T}_2 + p\hat{U}_2 &= \hat{M}_{22}\hat{T}_2 \end{aligned} \quad (28)$$

$$p\hat{U}_3 = \frac{m}{q}\hat{M}_{12}\hat{T}_2.$$

An FFT operation is performed to obtain $T_2(k, t)$ for the normal line load. The velocities with respect to the time in the x_1, x_2 and x_3 directions at all grid points are then calculated using Equation (28), which requires convolutions and inverse FFT operations. The displacements are obtained by integrating the velocities. A comparison between the numerical and analytical solutions is presented in Figure 3, which shows the evolution of the vertical displacement normal to the free surface and radial displacements parallel to the free surface at a point located at a distance r from the point of application of the force. It is observed that $\beta \leq 0.4$ is able to capture the singularity when the dilatational wave (P) arrives at observation point, as well as the change in

slope associated with the shear wave (S) and the Rayleigh wave (R). In the following, we choose $\beta = 0.4$ for the simulations. It is worth noting that oscillations are observed in the solutions, particularly near the singularity and the delta function, which can be attributed to the finite Fourier sum's inability to adequately represent a step or delta function.

Similar calculations are performed by obtaining radial and tangential displacement for the case B loading. In this case, the step horizontal line load is applied to an elastic half-space and is given by

$$\begin{aligned}\tau_1^0(x_1, x_3, t) &= P \sin(\theta) \delta(x_1) \delta(x_3) H(t) \\ \tau_3^0(x_1, x_3, t) &= P \cos(\theta) \delta(x_1) \delta(x_3) H(t) \\ \tau_2^0 &= 0,\end{aligned}\tag{29}$$

and the free surface conditions require that $\tau_1 = \tau_2 = \tau_3 = 0$. By substituting these conditions into Equation (16), we can obtain the elastodynamic equations for each Fourier mode as

$$\begin{aligned}\frac{c_s}{\mu} \hat{T}_1 - p \hat{U}_1 &= \frac{1}{q^2} (k^2 \hat{M}_{11} + m^2 \hat{M}_{33}) \hat{T}_1 + \frac{km}{q^2} (\hat{M}_{11} - \hat{M}_{33}) \hat{T}_3 \\ \frac{c_s}{\mu} \hat{T}_3 - p \hat{U}_3 &= \frac{km}{q^2} (\hat{M}_{11} - \hat{M}_{33}) \hat{T}_1 + \frac{1}{q^2} (m^2 \hat{M}_{11} + k^2 \hat{M}_{33}) \hat{T}_3.\end{aligned}\tag{30}$$

Figure 4 presents the radial and tangential displacements at the free surface caused by a horizontal line load, for stability parameter $\beta = 0.4$, and compared with the analytical solution. The results show excellent agreement with the analytical solution for the β value of 0.4, which validates the kernels. The accuracy and stability of the proposed scheme for bi-material interfaces are discussed in Section 3.2.

3.2 | 3D Lamb's Problem for a Bi-material Interface

In this section, we start with two separate cases when a pair of opposing normal and horizontal step line loads with P are applied just above and below a frictionless planar interface between two half-spaces having different properties, as illustrated in Figure 5. The elastic mismatch parameters are characterized by $c_s^-/c_s^+ = 1.2$ and $\mu^-/\mu^+ = 1.2$. Poisson's ratio is taken to be 0.25 for both solids.

The interfacial plane, which is of size $X * X$, is discretized into a 512 by 512 spatial grid, similar to the half-space discretization in the previous sub-section. The observation point is located at a distance of $r = \sqrt{x_1^2 + x_3^2}$ from the point of load application, with $x_1 = x_3 = X/8$.

We will first be examining Case A, which involves a pair of normal step line load acting on the interfacial plane, and is given by

$$\tau_2^0(x_1, x_3, t) = P\delta(x_1)\delta(x_3)H(t). \quad (31)$$

$$\tau_1^0 = \tau_3^0 = 0.$$

The free surface conditions are such that $\tau_1 = \tau_2 = \tau_3 = 0$. By substituting these values into Equation (16), we can obtain the elastodynamic equations for each Fourier mode as

$$\begin{aligned} p\widehat{D}_1 &= \widehat{C}_{12}\widehat{T}_2 \\ \frac{c_s^+}{\mu^+}\xi\widehat{T}_2 + p\widehat{D}_2 &= \widehat{C}_{22}\widehat{T}_2 \end{aligned} \quad (32)$$

$$p\widehat{D}_3 = \widehat{C}_{32}\widehat{T}_2.$$

In order to obtain $T_2(t; q)$ for the normal line load, an FFT operation is performed. The slip rate in the x_1 , x_2 and x_3 directions are then calculated at all grid points using Equation (32) and by

performing the convolutions indicated in the equation, as well as inverse FFT operations. The slip is subsequently calculated by integrating the slip rate. Figure 6 presents a direct comparison between the numerical and analytical solutions, showing the evolution of the vertical opening normal to the interfacial plane and the radial slip parallel to the planar interface at a specified point located at a distance r away from the point of force application. The results indicate that $\beta = 0.4$ is able to capture the singularities associated with the arrival of the dilatational wave (P), the change of slope associated with the shear wave (S), and the Rayleigh wave (R). The numerical solution for $\beta = 0.4$ shows good agreement between numerical and analytical solutions, validating kernels C_{12} and C_{22} . However, oscillations are observed in the solutions, particularly near the discontinuity and delta function, which can be attributed to the finite Fourier sum's inability to adequately represent a step or delta function. There are additional singularities corresponding to wave arrivals in different materials across the planar interface.

The calculations are similarly repeated to obtain radial and tangential slip for the case B loading.

In this case, a pair of horizontal line loads act on the planer interface, given by

$$\begin{aligned}\tau_1^0(x_1, x_3, t) &= P \sin(\theta) \delta(x_1) \delta(x_3) H(t) \\ \tau_3^0(x_1, x_3, t) &= P \cos(\theta) \delta(x_1) \delta(x_3) H(t) \\ \tau_2^0 &= 0.\end{aligned}\tag{33}$$

The free surface conditions are represented by $\tau_1 = \tau_2 = \tau_3 = 0$. Substituting these values into Equation (33) gives us the elastodynamic equations for each Fourier mode as

$$\frac{c_s^+}{\mu^+} \eta \hat{T}_1 + p \hat{D}_1 = \hat{C}_{11} \hat{T}_1 + \hat{C}_{13} \hat{T}_3$$

$$\frac{c_s^+}{\mu^+} \eta \hat{T}_3 + p \hat{D}_3 = \hat{C}_{31} \hat{T}_1 + \hat{C}_{33} \hat{T}_3. \quad (34)$$

Figure 7 shows the radial and tangential slips at the planar interface for stability parameters $\beta = 0.4$, and their comparison with the analytical solution. The results demonstrate that the proposed traction-based formulation is stable for bi-material interfaces. This conclusion is supported by the excellent agreement between the numerical and analytical solutions for $\beta = 0.4$, which validates the remaining kernels.

For simulation of dynamic ruptures, the BIE scheme needs to be coupled with a friction law. In Sections 4 and 5, new algorithms are proposed for coupling the BIE with a slip-weakening friction law for 2D and 3D problems, respectively. The scheme is then applied to simulate frictional rupture propagation and validated using benchmark problems from the Southern California Earthquake Center.

4 | Spontaneous 2D in-plane rupture propagation

This section presents an investigation of 2D dynamic rupture propagation at the interface between two elastic half-planes. The proposed approach couples a 2D in-plane spectral BIE method with a frictional constitutive law at the interface. However, to demonstrate the potential of this numerical scheme, two fracture problems are presented. The first problem involves a dynamic rupture simulation on a fault between identical solids with heterogeneous initial shear stress distribution. The problem parameters are based on the SCEC Benchmark Validation exercises. The second problem is a dynamic rupture simulation at a bi-material fault, demonstrating the current method's adequacy, flexibility, and superior performance for problems involving heterogeneity across the interface. Previous analytical studies have shown that steady sliding of dissimilar elastic half-planes with a Coulomb friction law at the interface is ill-posed.^{16,17} They observed a short-

wavelength instability for arbitrarily small values of the friction coefficient when the in-plane slip wave was present for the pair of elastic materials forming the interface, indicating an ill-posed stability problem. A comparison of the numerical results obtained for the second problem using the proposed approach with the theoretical predictions of analytical studies is presented here.

4.1 | A benchmark problem TPV205-2D for earthquake rupture in an unbounded homogeneous domain.

The present approach has been verified through the utilization of the TPV205-2D benchmark problem, which is part of the SCEC Dynamic Rupture Validation exercises. In this benchmark problem, a 2D inplane slip-weakening fault is embedded in a linear-elastic homogeneous bulk under plane strain conditions (see Figure 8a). The material properties, including the shear and dilatational wave speeds and density, are identical on both sides of the interface. They are taken as $c_s^+ = c_s^- = c_s = 3464 \text{ m/s}$, $c_d^+ = c_d^- = c_d = 6000 \text{ m/s}$ and $\rho^+ = \rho^- = \rho = 2670 \text{ kg/m}^3$, respectively. The interfacial length, $L = 100 \text{ km}$, is discretized into $N_{ele} = 8192$ elements with a spatial discretization size of $\Delta x = L/N_{ele}$, and the time step corresponds to $\Delta t = 0.4 \Delta x/c_s$. The rupture is nucleated by overstressing a wide region of 3 km situated at the center of the fault. Figure 8 (b) shows the initial shear stress on the fault, τ_1^0 . Two high-strength barriers with a length of $L_s = 35 \text{ km}$ on each side are located on both edges of the fault. The static frictional strength is set to a high value in these regions to prevent the rupture from propagating there. A uniform background shear stress of $\tau_1^0 = 70 \text{ MPa}$ and uniform normal stress of $\tau_2^0 = -120 \text{ MPa}$ are applied throughout the simulation. Hence, the peak friction strengths $\tau_s = 81.24 \text{ MPa}$ and dynamic friction strengths $\tau_s = 63 \text{ MPa}$ also remain constant, from Equation (26). The BIE for this problem follows from Equation (12),

$$\frac{2c_s}{\mu}T_1(t; q) + \frac{\partial D_1(t; q)}{\partial t} = F_1(t; q) \equiv 2 \int_0^t M_{11}(t; q) T_1(t - t'; q) dt'. \quad (35)$$

The slip weakening friction law given by Equation (26) is coupled with the above BIE to simulate the dynamic rupture at the interface. An algorithm is developed to implement the friction law at the interface numerically, and it is provided in Algorithm 1.

Algorithm 1. 2D update algorithm for an interface between identical solids

- Step (i)* Set the initial values of slip, δ_1 , slip rate, $\dot{\delta}_1$, and shear stress, τ_1 , to zero prior to the nucleation process.
- Step (ii)* Determine $T_1(t - \Delta t; q)$ by performing FFT on $\tau_1(x_1, t - \Delta t) - \tau_1^0$.
- Step (iii)* Evaluate $F_1(t; q)$. (Notice that $T_1(t; q)$ does not contribute to the convolution integral, Equation (35), at the current time due to the vanishing of the convolution kernels at zero, $M_{11}(0; q) = 0$).
- Step (iv)* Apply the inverse FFT and from Equation (13), determine the value at the current time of $\frac{2c_s}{\mu}(\tau_1(x_1, t) - \tau_1^0(x_1, t)) + \dot{\delta}_1(x_1, t)$.
- Step (v)* Get current slip, $\delta_1(x_1, t) = \delta_1(x_1, t - \Delta t) + \dot{\delta}_1(x_1, t - \Delta t)\Delta t$, using forward Euler method.
- Step (vi)* Update the frictional strength, $\tau_{str}(x_1, t)$, from Equation (26).
- Step (vii)* Determine the shear stress, $\tau_1(x_1, t)$, and the slip velocity, $\dot{\delta}_1(x_1, t)$, at current time by solving the first equation of Equation (13) and the friction law, Equation (26) simultaneously, using following possible conditions:
- a) **If** ($\delta_1 < \delta_c$) **then**
-

-
- b) **If** $\left(\tau_{str} > \tau_1^0 + f_1 \frac{\mu}{2c_s}\right)$ **then**
 - c) Stick state.
 - d) Update $\dot{\delta}_1 = 0, \tau_1(x_1, t) = \tau_1^0 + f_1(x_1, t) \frac{\mu}{2c_s}$.
 - e) **Else**
 - f) Slip state.
 - g) Update $\tau_1 = \tau_{str}, \dot{\delta}_1 = (\tau_1^0 - \tau_{str}) \frac{2c_s}{\mu} + f_1(x_1, t)$.
 - h) **End if**
 - i) **Else**
 - j) Update $\tau_1 = \tau_d, \dot{\delta}_1 = (\tau_1^0 - \tau_d) \frac{2c_s}{\mu} + f_1(x_1, t)$
 - k) **End if**
-

The current numerical scheme is applied to solve the TPV205-2D benchmark problem and the obtained results are compared with the SCEC benchmark results.³⁸ Figure 9 presents slip and slip rate at the interface at one-second intervals from $t = 1$ s to $t = 5$ s. The simulation accurately captures the different stages of rupture, including nucleation, propagation, and arrest. Figure 10 shows the comparison of the results obtained from the current approach with those from the benchmark. Specifically, Figure 10 display time history plots of slip, slip rate, and shear traction for a time period of 6 seconds at a point located at the center of the fault (denoted by A) and at a distance of 4.5 km from the center (denoted by B), respectively. The results obtained here are in excellent agreement with the results of the benchmark, thereby providing further validation for the current numerical scheme.

4.2 | Bi-material interface

Following the successful validation of the proposed method with the SCEC benchmark problem TPV205-2D, we proceed to conduct a numerical analysis using the BIE in conjunction with a frictional constitutive law at a bi-material interface. The interface is subject to slip-weakening friction. The model geometry, depicted in Figure 11, involves a fault of length $L = 100 \text{ km}$ that is discretized into N_{ele} elements with spatial discretization size $\Delta x = L/N_{ele}$, and a time step size of $\Delta t = 0.4 \Delta x / \max(c_s^+, c_s^-)$. The fault is bounded on its left and right edges by strength barriers, each with a length of $L_s = 30 \text{ km}$. These barriers are considered to be bonded regions with static frictional strength that is high enough to prevent rupture propagation there. The initial shear stress, $\tau_1^0 = 70 \text{ MPa}$, is uniform along the fault plane except for a central patch of length $L_{nuc} = 3 \text{ km}$, where it is overstressed as $\tau_{nuc} = 81.6 \text{ MPa}$ to induce abrupt nucleation of a dynamic event. The normal stress is initially uniform along the entire fault length, with peak and dynamic friction strengths of $\tau_s = 81.24 \text{ MPa}$ and $\tau_d = 63 \text{ MPa}$, respectively. As time progresses ($t > 0$), nonuniform in-plane slip induces changes in normal stress due to a mismatch of elastic properties across the fault, thereby affecting the peak and residual friction strengths. Therefore, the BIE for this problem will follow from Equation (12),

$$\left\{ \begin{array}{l} \frac{c_s^+}{\mu^+} \eta T_1(t; q) + \frac{\partial D_1(t; q)}{\partial t} \\ \frac{c_s^+}{\mu^+} \xi T_2(t; q) \end{array} \right\} = \begin{Bmatrix} F_1(t; q) \\ F_3(t; q) \end{Bmatrix}, \quad (36)$$

where convolution terms are given by

$$\begin{Bmatrix} F_1(t; q) \\ F_2(t; q) \end{Bmatrix} = \int_0^t \begin{bmatrix} M_{11}^+(t'; q) + M_{11}^-(t'; q) & M_{12}^+(t'; q) - M_{12}^-(t'; q) \\ M_{21}^+(t'; q) - M_{21}^-(t'; q) & M_{22}^+(t'; q) + M_{22}^-(t'; q) \end{bmatrix} \begin{Bmatrix} T_1(t - t'; q) \\ T_2(t - t'; q) \end{Bmatrix} dt'.$$

Additionally, an algorithm has been created to implement the friction law numerically at the bi-material interface. It is described in Algorithm 2.

Algorithm 2: 2D update algorithm for a bi-material interface

- Step (i)* Set the initial values of slip, δ_1 , slip rate, $\dot{\delta}_1$, and shear stress, τ_1 , to zero prior to the nucleation process.
- Step (ii)* Determine $T_i(t - \Delta t; q)$ by performing FFT on $\tau_i(x_1, t - \Delta t) - \tau_i^0$, where ($i = 1, 2$).
- Step (iii)* Evaluate first prediction of $F_i^*(t; q)$ at current time by assuming $T_i(t; q) = T_i(t - \Delta t; q)$.
- Step (iv)* Apply the inverse FFT and use Equation (13) to determine the value at the current time step of the following quantities:

$$\tau_1^*(x_1, t) - \tau_1^0(x_1, t) + \frac{\mu^+}{c_s^+} \frac{1}{\eta} \dot{\delta}_1^*(x_1, t) = f_1^*(x_1, t) \frac{\mu^+}{c_s^+} \frac{1}{\eta}$$

$$\tau_2^*(x_1, t) - \tau_2^0(x_1, t) = f_2^*(x_1, t) \frac{\mu^+}{c_s^+} \frac{1}{\xi}$$

(Note that imposing no opening condition at the planar interface will lead to $\dot{\delta}_2 = 0$)

- Step (v)* Get current shear slip, $\delta_1^*(x_1, t) = \delta_1(x_1, t - \Delta t) + \dot{\delta}_1(x_1, t - \Delta t)\Delta t$, using forward Euler method:
-

Step (vi) Update the frictional strength, $\tau_{str}^*(x_1, t)$, from Equation (26).

Step (vii) Determine the shear stress, $\tau(x_1, t)$, and the slip velocity, $\dot{\delta}_1(x_1, t)$, at current time by solving *step (iv)* and the friction law, Equation (26), simultaneously using following possible conditions:

Step (viii)

a. **If** ($\delta_1^* < \delta_c$) **then**

b. **If** ($\tau_{str}^* > \tau_1^0 + f_1^* \frac{\mu^+ 1}{c_s^+ \eta}$) **then**

c. Stick state.

d. Update $\dot{\delta}_1^* = 0$.

e. Update $\tau_2^*(x_1, t) = \tau_2^0 + f_2^*(x_1, t) \frac{\mu^+ 1}{c_s^+ \xi}$.

f. Update $\tau_1^*(x_1, t) = \tau_1^0 + f_1^*(x_1, t) \frac{\mu^+ 1}{c_s^+ \eta}$.

g. **Else**

h. Slip state.

i. Update $\tau_2^*(x_1, t) = \tau_2^0 + f_2^*(x_1, t) \frac{\mu^+ 1}{c_s^+ \xi}$.

j. Update $\tau_1^* = -f_{str} \tau_2^*$.

k. Update $\dot{\delta}_1^* = (\tau_1^0 - \tau_1^*) \frac{c_s^+}{\mu^+} \eta + f_1^*(x_1, t)$.

l. **End if**

m. **Else**

n. Update $\tau_2^*(x_1, t) = \tau_2^0 + f_2^*(x_1, t) \frac{\mu^+ 1}{c_s^+ \xi}$.

o. Update $\tau_1^* = -f_d \tau_2^*$.

p. Update $\dot{\delta}_1^* = (\tau_1^0 - \tau_1^*) \frac{c_s^+}{\mu^+} \eta + f_1^*(x_1, t)$.

q. End if

Step (ix) Determine $T_i^*(t; q)$ by performing FFT on $\tau_i^*(x_1, t) - \tau_i^0$.

Step (x) Evaluate $F_i^{**}(t; q)$ and perform inverse FFT.

Step (xi) Update $\delta_1^{**}(x_1, t) = \delta_1(x_1, t - \Delta t) + (\dot{\delta}_1(x_1, t - \Delta t) + \dot{\delta}_1^*(x_1, t))\Delta t/2$.

Step (xii) Evaluate $\tau_1^{**}(x_1, t)$, $\tau_2^{**}(x_1, t)$ and $\dot{\delta}_1^{**}(x_1, t)$ by performing *steps (iv), (vi), (vii)* sequentially.

The numerical results focus on two scenarios with different elastic mismatch parameters: (a) $c_s^-/c_s^+ = 2$ and $\rho^-/\rho^+ = 1.2$, and (b) $c_s^-/c_s^+ = 1.2$ and $\rho^-/\rho^+ = 1.2$; while keeping fixed material properties of top half-space as $c_s^+ = 3464 \text{ m/s}$, $c_d^+ = 6000 \text{ m/s}$ and $\rho^+ = 2670 \text{ kg/m}^3$. For first scenario, Figures. 12 (a) and 12 (b) illustrates the slip and slip rate at the interface at one-second time intervals, starting from $t = 1 \text{ s}$ and ending at $t = 5 \text{ s}$. The rupture begins at the center, and it propagates in the direction of motion of the softer material, referred to as the 'positive' direction. The rupture speed approaches the shear wave velocity of the softer material in this direction. On the other hand, in the 'negative' direction, where the motion of the softer material is opposite to the rupture direction, the rupture speed is slightly below the P-wave velocity of the softer material. Given the dynamic nature of the problem, the temporal evolution of the field quantities, such as shear stress and slip rate, is also presented at two stations, A and B, for a period of six seconds in Figure 13, respectively. These stations are located at the fault's center and 4.5 km away from it, respectively. The second scenario, where the elastic mismatch parameters are defined as $c_s^-/c_s^+ = 1.2$ and $\rho^-/\rho^+ = 1.2$, shows instabilities in the slip and slip rate (see Figure 14) as time evolves.

This is due to the ill-posed nature of the problem for this combination of elastic mismatch parameters, which results in short wavelength instabilities as predicted by Ranjith and Rice.¹⁶ These instabilities do not occur in the first scenario and make the problem ill-posed. Similar to the first scenario, the temporal evolution of the field quantities (slip, slip rate and shear stress) at two points A and B are shown for a time period of 6 seconds in Figure 15, respectively. The results show that as time evolves, the field quantities become unstable due to the ill-posed nature of this case.

5 | Spontaneous 3D rupture propagation

This section focuses on the investigation of 3D dynamic rupture propagation at a bi-material interface using the proposed 3D spectral BIE coupled with a frictional constitutive law. To showcase the versatility of the current numerical scheme, two fracture problems are presented. The first one involves the use of SCEC Benchmark Validation exercises while the second problem deals with a bi-material fault.

5.1 | BENCHMARK PROBLEM TPV3: EARTHQUAKE RUPTURE IN UNBOUNDED HOMOGENEOUS DOMAIN

The current method is verified using Exercise TPV3 from the SCEC Dynamic Rupture Validation exercises. This problem involves a planar fault with linear slip-weakening friction that is embedded in a homogeneous linear elastic bulk, as shown in Figure 16. Both sides of the planar fault have the same material properties, with the shear and dilatational wave speed and density of both top and bottom half-planes taken as $c_s^+ = c_s^- = c_s = 3464$ m/s and $c_d^+ = c_d^- = c_d = 6000$ m/s and $\rho^+ = \rho^- = \rho = 2670$ kg/m³, respectively. The fracture plane has an area of $L_1 *$

$L_3 = 45 \text{ km} * 22.5 \text{ km}$ and is discretized using $N_{ele} * N_{ele}/2$ square grid elements with the same spatial discretization size, $\Delta x_1 = \Delta x_3 = L_1/N_{ele}$. The time step used in the simulation corresponds to $\Delta t = 0.4 \Delta x_1/c_s$. To initiate the rupture, the shear stress, $\tau_{nuc} = 81.6 \text{ MPa}$, is instantaneously increased to a value higher than the static friction on a square patch of size $3 \text{ km} * 3 \text{ km}$ located at the center of the fault. The rupture then quickly propagates across the entire fault. A uniform background shear stress, $\tau_1^0 = 70 \text{ MPa}$ is applied along the x_1 - direction over the fracture plane, while the normal stress acting on the fault remains unchanged during the entire simulation. The peak and residual friction strengths also remain constant. Two strength barriers with a length of $L_1^s = 7.5 \text{ km}$ and $L_3^s = 3.5 \text{ km}$ are located on each side of the planar fault along the x_1 - and x_3 - directions. These barriers have a high enough static frictional strength to prevent the rupture from propagating further. The BIE for this problem will follow from Equation (19),

$$\left\{ \begin{array}{l} \frac{2c_s}{\mu} T_1(t; k, m) + \frac{\partial D_1(t; k, m)}{\partial t} \\ \frac{2c_s}{\mu} T_3(t; k, m) + \frac{\partial D_3(t; k, m)}{\partial t} \end{array} \right\} = \left\{ \begin{array}{l} F_1(t; k, m) \\ F_3(t; k, m) \end{array} \right\} \quad (37)$$

where,

$$\left\{ \begin{array}{l} F_1(t; k, m) \\ F_3(t; k, m) \end{array} \right\} = \int_0^t \left[\begin{array}{cc} F_{11}(t'; q) & F_{13}(t'; q) \\ F_{31}(t'; q) & F_{33}(t'; q) \end{array} \right] \left\{ \begin{array}{l} T_1(t - t'; k, m) \\ T_3(t - t'; k, m) \end{array} \right\} dt'.$$

A slip weakening friction law, Equation (26), is then combined with the aforementioned BIE to simulate dynamic rupture at the interface. An algorithm, outlined in Algorithm 3, is developed to implement the friction law numerically at the interface.

Algorithm 3: 3D update algorithm for an interface between identical solids

Step (i) Set the initial values of slip, δ_i , slip rate, $\dot{\delta}_i$, and shear stress, τ_i , to zero prior to the nucleation process, where ($i = 1, 3$).

Step (ii) Determine $T_i(t - \Delta t; k, m)$ by performing FFT on $\tau_i(x_1, x_3, t - \Delta t) - \tau_i^0$, where ($i = 1, 3$).

Step (iii) Evaluate $F_i(t; k, m)$. (Notice that at the current time $T_i(t, k, m)$ does not contribute to the convolution integral, Equation (37), due to the vanishing of the convolution kernels at zero, $F_{ij}(0; q) = 0$, where, $i, j = 1, 3$).

Step (iv) Apply the inverse FFT and use Equation (6) to determine the value at the current time step of the following quantities:

$$\psi_i = \tau_i^0 + f_i(x_1, x_3, t) \frac{\mu}{2c_s}$$

$$\psi = \sqrt{\psi_1^2 + \psi_3^2}.$$

Step (v) Get current slip using forward Euler method:

$$\delta_i(x_1, x_3, t) = \delta_i(x_1, x_3, t - \Delta t) + \dot{\delta}_i(x_1, x_3, t - \Delta t)\Delta t,$$

$$\dot{\delta}_s(x_1, x_3, t - \Delta t) = \sqrt{\dot{\delta}_1^2 + \dot{\delta}_3^2},$$

$$\delta_s(x_1, x_3, t - \Delta t) = \sqrt{\delta_1^2 + \delta_3^2},$$

$$\delta_s(x_1, x_3, t) = \delta_s(x_1, x_3, t - \Delta t) + \dot{\delta}_s(x_1, x_3, t - \Delta t)\Delta t.$$

Step (vi) Update the frictional strength, $\tau_{str}(x_1, x_3, t)$, from Equation (26).

Step (vii) Determine the shear stress, $\tau_i(x_1, x_3, t)$ and the slip velocity, $\dot{\delta}_i(x_1, x_3, t)$ at current time by solving Equation (6) and the friction law, Equation (26), simultaneously using following possible conditions:

-
- a) **If** $(\delta_s < \delta_c)$ **then**
 - b) **If** $(\tau_{str} > \psi)$ **then**
 - c) Stick state.
 - d) Update $\dot{\delta}_s = 0 \equiv \dot{\delta}_i = 0$, $\tau_i(x_1, x_3, t) = \tau_i^0 + f_i(x_1, x_3, t) \frac{\mu}{2c_s}$.
 - e) **Else**
 - f) Slip state.
 - g) Update $\tau = \sqrt{\tau_1^2 + \tau_3^2} = \tau_{str}$
 - h) Solving proportionality ratio, $\dot{\delta}_i = \dot{\delta}_s \frac{\tau_i}{\tau_{str}}$, *step (iv)* and BIE Equation (37)

simultaneously, update the following field quantities:

- i. $\tau_i(x_1, x_3, t) = \tau_{str} \frac{\psi_i}{\psi}$,
- ii. $\dot{\delta}_i = (\tau_i^0 - \tau_{str}) \frac{2c_s}{\mu} + f_i(x_1, x_3, t)$.

- i) **End if**
- j) **Else**
- k) Update $\tau = \sqrt{\tau_1^2 + \tau_3^2} = \tau_d$,
- l) Solving proportionality ratio, $\dot{\delta}_i = \dot{\delta}_s \frac{\tau_i}{\tau_{str}}$, *step (iv)* and BIE Equation (37)

simultaneously, update the following field quantities:

- i. $\tau_i(x_1, x_3, t) = \tau_d \frac{\psi_i}{\psi}$,
- ii. $\dot{\delta}_i = (\tau_i^0 - \tau_d) \frac{2c_s}{\mu} + f_i(x_1, x_3, t)$.

- m) **End if**
-

We applied the current scheme to the TPV3 benchmark of SCEC and compared the results with those of the benchmark.³⁹ Our simulations showed that after the nucleation process, the rupture front rapidly expanded radially and eventually covered the entire fault area, as illustrated in Figure 17. Furthermore, we observed that the dynamic rupture emitted elastic waves, as expected. To demonstrate the temporal evolution of the field quantities (slip rate, shear stress), we plotted the results at two stations (A - 3 km away from the center along x_3 , B - 7.5 km away from the center along x_1) for a duration of 6 seconds, as shown in Figs. 18. At the onset of the rupture, the slip rate was zero at all stations since the waves had not yet arrived. As the rupture reached stations A, and B, the shear stress increased rapidly and then remained approximately constant as the fault continued to slide, until reflected waves from the boundary between the rupture region and the bonded region arrived at the stations. At this point, we observed a drop in the slip rate first at station A. Our simulation results matched well with the expected outcomes, validating the current scheme further. This problem runs over 1182 time steps, and takes a wall time of 4 min 45 s on a Nvidia DGX-1 system using a single Tesla V100 GPU.

5.2 | Bi-material interface

Upon successful validation of the current method with the SCEC benchmark problem TPV3, a numerical analysis is conducted using the proposed SBI method together with a slip-weakening frictional constitutive law at the interface. The study focuses on a bi-material interface governed by slip-weakening friction where the materials on either side of the planar fault are different. The geometry of the model is presented in Figure 19. The elastic mismatch parameters are characterized by $c_s^-/c_s^+ = 2$ and $\rho^-/\rho^+ = 1.2$ with $c_s^- = 3464 \text{ m/s}$ and $\rho^- = 2670 \text{ kg/m}^3$. The fault parameters are same as those used in TPV3 benchmark problem. The initial shear stress is

uniform over the fracture plane except for a central square patch where the fault is overstressed to initiate the dynamic event abruptly. The normal stress is initially uniform over the entire fault plane, and the initial peak and residual friction strengths are τ_s and τ_d . As time progresses ($t > 0$), the mismatch of elastic properties across the fault induces changes in normal stress during spatially nonuniform in-plane slip, and consequently the peak and residual friction strengths also vary. To simulate the dynamics of rupture at the bi-interface, a slip weakening friction law given by Equation (26) is coupled with the BIE equation (19). An algorithm is developed to implement the friction law numerically at the interface, which is presented in Algorithm 4.

Algorithm 4: 3D update algorithm for a bi-material interface

- Step (i)* Initial slip, δ_i , slip rate, $\dot{\delta}_i$, ($i = 1, 3$), and shear stress, τ_j , ($j = 1, 2, 3$), are all assumed zero.
- Step (ii)* Determine $T_i(t - \Delta t; k, m)$ by performing FFT on $\tau_i(x_1, x_3, t - \Delta t) - \tau_i^0$, where ($i = 1, 2, 3$).
- Step (iii)* Evaluate first prediction of $F_i^*(t; k, m)$ at current time by assuming $T_i(t; k, m) = T_i(t - \Delta t; k, m)$
- Step (iv)* Apply the inverse FFT and use Equation (6) to determine the value at the current time step of the following quantities:

$$\psi_i^* = \tau_i^0 + f_i^*(x_1, x_3, t) \frac{\mu^+}{c_s^+} \frac{1}{\eta}, \quad (i = 1, 3).$$

$$\psi^* = \sqrt{\psi_1^{*2} + \psi_3^{*2}}.$$

- Step (v)* Get current slip using forward Euler method:
-

$$\delta_i^*(x_1, x_3, t) = \delta_i(x_1, x_3, t - \Delta t) + \dot{\delta}_i(x_1, x_3, t - \Delta t)\Delta t,$$

$$\dot{\delta}_s^*(x_1, x_3, t - \Delta t) = \sqrt{\dot{\delta}_1^{*2} + \dot{\delta}_3^{*2}},$$

$$\delta_s(x_1, x_3, t - \Delta t) = \sqrt{\delta_1^2 + \delta_3^2},$$

$$\delta_s^*(x_1, x_3, t) = \delta_s(x_1, x_3, t - \Delta t) + \dot{\delta}_s^*(x_1, x_3, t - \Delta t)\Delta t.$$

Step (vi) Update the frictional strength, $\tau_{str}^*(x_1, x_3, t)$, from Equation (26).

Step (vii) Determine the shear stress, $\tau_i^*(x_1, x_3, t)$ and the slip velocity, $\dot{\delta}_i^*(x_1, x_3, t)$ at current time by solving Equation (6) and the friction law, Equation (26), simultaneously using following possible conditions:

- a) **If** ($\delta_s^* < \delta_c$) **then**
 - b) **If** ($\tau_{str}^* > \psi^*$) **then**
 - c) Stick state.
 - d) Update, $\dot{\delta}_s^* = 0 \equiv \dot{\delta}_i^* = 0$.
 - e) Update, $\tau_1^*(x_1, x_3, t) = \tau_1^0 + f_1^*(x_1, x_3, t) \frac{\mu^+}{c_s^+} \frac{1}{\eta}$.
 - f) Update, $\tau_2^*(x_1, x_3, t) = \tau_2^0 + f_2^*(x_1, x_3, t) \frac{\mu^+}{c_s^+} \frac{1}{\xi}$.
 - g) Update, $\tau_3^*(x_1, x_3, t) = \tau_1^0 + f_3^*(x_1, x_3, t) \frac{\mu^+}{c_s^+} \frac{1}{\eta}$.
 - h) **Else**
 - i) Slip state.
 - j) Update $\tau_{str}^* = \sqrt{\tau_1^{*2} + \tau_3^{*2}} = -f_{str}\tau_2^*$
-

k) Solving proportionality ratio, $\dot{\delta}_i^* = \dot{\delta}_s^* \frac{\tau_i^*}{\tau_{str}^*}$, *step (iv)* and BIE Equation (6)

simultaneously, update the following field quantities:

i. $\tau_i^*(x_1, x_3, t) = \tau_{str}^* \frac{\psi_i^*}{\psi^*}.$

ii. $\tau_2^*(x_1, t) = \tau_2^0 + f_2^*(x_1, t) \frac{\mu^+ 1}{c_s^+ \xi}.$

iii. $\dot{\delta}_i^* = (\tau_i^0 - \tau_i^*) \frac{c_s^+}{\mu^+} \eta + f_i^*(x_1, x_3, t).$

l) **End if**

m) **Else**

n) Update $\tau_d^* = \sqrt{\tau_1^{*2} + \tau_3^{*2}} = -f_d \tau_2^*$

o) Solving proportionality ratio, $\dot{\delta}_i^* = \dot{\delta}_s^* \frac{\tau_i^*}{\tau_{str}^*}$, *step (iv)* and BIE Equation (6)

simultaneously, update the following field quantities:

i. $\tau_i^*(x_1, x_3, t) = \tau_d^* \frac{\psi_i^*}{\psi^*}.$

ii. $\tau_2^*(x_1, t) = \tau_2^0 + f_2^*(x_1, t) \frac{\mu^+ 1}{c_s^+ \xi}.$

iii. $\dot{\delta}_i^* = (\tau_i^0 - \tau_i^*) \frac{c_s^+}{\mu^+} \eta + f_i^*(x_1, x_3, t).$

p) **End if**

Step (viii) Determine $T_i^*(t; k, m)$ by performing FFT on $\tau_i^*(x_1, x_3, t) - \tau_i^0$.

Step (ix) Evaluate $F_i^{**}(t; k, m)$ and perform inverse FFT.

Step (x) Evaluate $\delta_i^{**}(x_1, x_3, t) = \delta_i(x_1, x_3, t - \Delta t) + (\dot{\delta}_i(x_1, x_3, t - \Delta t) + \dot{\delta}_i^*(x_1, x_3, t))\Delta t/2$.

Step (xi) Evaluate $\tau_1^{**}(x_1, x_3, t)$, $\tau_2^{**}(x_1, x_3, t)$ and $\dot{\delta}_1^{**}(x_1, x_3, t)$ by performing *steps (iv)*, *(vi)*, *(vii)* sequentially.

Numerical results are obtained and presented in Figure 20, depicting the slip and slip rate at the interface at time intervals of one second, ranging from $t = 1$ s to $t = 5$ s. The nucleation event occurred at the center, causing the rupture front to rapidly propagate radially and eventually span the entire fault (see Figure 20). The speed of the rupture front in the positive direction (both rupture and softer material's motion direction are same) approached the shear wave velocity of the softer material, while in the 'negative' direction (when motion of the softer material is opposite the rupture direction), the rupture speed was slightly below the P-wave velocity of the softer material. These observations are consistent with the results obtained in the 2D problem discussed in previous section. To account for the dynamic nature of the problem, the temporal evolutions of shear stress and slip rate for a duration of 6 seconds are also examined at two stations, A and B (as seen in Figure 21), located 3 km away from the center along x_3 and 7.5 km away from the center along x_1 , respectively. This problem runs over 1182 time steps, and takes a wall time of 19 min 45 s on a Nvidia DGX-1 system using a single Tesla V100 GPU.

6 | Discussion

This paper presents the derivation of convolution kernels used in a 3D spectral formulation of the boundary integral equations for an interface between two dissimilar elastic half-spaces. These

convolution kernels, along with a constitutive law for the interface, can be utilized to simulate dynamic ruptures at the interface between two elastic solids. The following section demonstrates a comparison between the proposed method and the one proposed by Breitenfeld and Geubelle:³³

1. Breitenfeld and Geubelle³³ proposed an "independent" formulation where spectral elastodynamic analysis is performed separately for each half-space as

$$\begin{pmatrix} T_1(t; k, m) \pm \frac{\mu^\pm}{c_s^\pm} \frac{\partial U_1^\pm(t; k, m)}{\partial t} \\ T_2(t; k, m) \pm \frac{c_d^\pm}{c_s^\pm} \frac{\mu^\pm}{c_s^\pm} \frac{\partial U_2^\pm(t; k, m)}{\partial t} \\ T_3(t; k, m) \pm \frac{\mu^\pm}{c_s^\pm} \frac{\partial U_3^\pm(t; k, m)}{\partial t} \end{pmatrix} = \begin{pmatrix} G_1^\pm(t; k, m) \\ G_2^\pm(t; k, m) \\ G_3^\pm(t; k, m) \end{pmatrix} \quad (38)$$

where "+" refer to top half-space and "-" refer to bottom half-space. In the above equation, convolution terms are given by

$$\begin{aligned} & \begin{pmatrix} G_1^\pm(t; k, m) \\ G_2^\pm(t; k, m) \\ G_3^\pm(t; k, m) \end{pmatrix} \\ &= -i\mu^\pm \left(2 - \frac{c_d^\pm}{c_s^\pm} \right) \begin{pmatrix} 0 & -k & 0 \\ k & 0 & m \\ 0 & -m & 0 \end{pmatrix} \begin{pmatrix} U_1^\pm(t - t'; k, m) \\ U_2^\pm(t - t'; k, m) \\ U_3^\pm(t - t'; k, m) \end{pmatrix} \\ &- i\mu^\pm q \int_0^t \begin{pmatrix} \pm \frac{H_{11}(qc_s^\pm t')k^2 + H_{33}(qc_s^\pm t')m^2}{q^2} & -ik \frac{H_{12}(qc_s^\pm t')}{|q|} & \pm \frac{(H_{11}(qc_s^\pm t') - H_{33}(qc_s^\pm t'))km}{q^2} \\ ik \frac{H_{12}(qc_s^\pm t')}{|q|} & \pm H_{22}(qc_s^\pm t') & -im \frac{H_{12}(qc_s^\pm t')}{|q|} \\ \pm \frac{(H_{11}(qc_s^\pm t') - H_{33}(qc_s^\pm t'))km}{q^2} & -im \frac{H_{12}(qc_s^\pm t')}{|q|} & \pm \frac{H_{11}(qc_s^\pm t')m^2 + H_{33}(qc_s^\pm t')k^2}{q^2} \end{pmatrix} \\ & \quad * \begin{pmatrix} U_1^\pm(t - t'; k, m) \\ U_2^\pm(t - t'; k, m) \\ U_3^\pm(t - t'; k, m) \end{pmatrix} dt', \end{aligned}$$

where H_{ij} are convolution kernels. It may be noted that the solution of the bi-material rupture problem, in its most comprehensive form, requires the computation of 18 convolution integrals as shown in Equation (38). In contrast to Breitenfeld and Geubelle's "independent" formulation, the proposed approach performs elastodynamic convolution on the interface's shear stress history at each time instant, as shown in Equation (19). This method reduces the number of convolution integrals required from eighteen to nine, resulting in a significant decrease in computation time. The proposed method is expected to save at least 50% of computation time when compared to the method of Breitenfeld and Geubelle.³³

2. In Breitenfeld and Geubelle's³³ "independent" formulation, all convolution kernels H_{11} , H_{22} and H_{33} except H_{12} are expressed in closed form because of the complicated Laplace transform of that kernel. Thus, the convolution kernel H_{12} is obtained numerically by inverting the Laplace transform of the kernel. In contrast, the proposed approach overcomes this limitation of the formulation of Breitenfeld and Geubelle³³ by allowing all convolution kernels in closed form, thereby increasing numerical efficiency.
3. Breitenfeld and Geubelle³³ also proposed the "combined" formulation for the bi-material problem, in which convolutions were performed on the history of interfacial displacement discontinuities, resulting in 9 convolutions. However, they reported that this method was numerically less stable compared to the "independent" formulation and did not provide any results with the "combined" formulation. Moreover, none of the convolution kernels for the "combined" formulation could be expressed in closed form. In contrast, in the present method all convolution kernels are expressed in closed form and the numerical method is stable.

7 | Conclusions:

A new spectral scheme has been developed to study dynamic fracture problems in two and three dimensions. Spontaneous planar crack propagation in response to applied loads under the action of interfacial constitutive laws can be studied using the numerical scheme. The proposed method uses elastodynamic convolutions of the traction components of stress at the interface between the half-spaces. This is in contrast to previous studies that used convolutions of the displacements or displacement discontinuities at the interface. The convolution kernels used in the method are derived. Due to continuity of tractions at the interface, the convolution kernels take a simple form. The convolution kernels are validated by comparing numerical solutions to the 3D Lamb problem with existing analytical solutions. Algorithms are designed for the study of 2D and 3D slip rupture propagation at a bi-material interface with a slip-weakening friction law at the interface. The algorithms are validated using some benchmark problems from the Southern California Earthquake Center (SCEC). Finally, the method is applied to simulate 3D frictional rupture propagation along a bi-material interface.

Declaration of competing interest

The authors declare that they have no known competing financial interests or personal relationships that could have appeared to influence the work reported in this paper.

Acknowledgement

This work is supported by National Supercomputing Mission, India under grant no. DST/NSM/R&D_HPC_Applications/2021/02.

Data availability statement

Data available on request.

Appendix A

As described in Section 2.1, the convolution kernels $M_{11}(t; q)$, $M_{12}(t; q)$, $M_{22}(t; q)$ and $M_{33}(t; q)$ can be calculated from their Laplace transforms (Equation (11)), which are given by Ranjith (2015, 2022) as

$$\begin{aligned}
 M_{11}(t; q) = c_s |q| \frac{c_s}{\mu} & \left\{ - \int_0^1 \frac{g(y) - g(y_R)}{y - y_R} y \sin(|q| c_s t) dy \right. \\
 & + g(y_R) \left[y_R \sin(|q| c_R t) \int_{(|q| c_s t - |q| c_R t)}^{|q| c_R t} \frac{\cos \theta}{\theta} d\theta \right. \\
 & \left. \left. - y_R \cos(|q| c_R t) \int_{-|q| c_R t}^{(|q| c_s t - |q| c_R t)} \frac{\sin \theta}{\theta} d\theta \right] + g(y_R) \frac{\cos(|q| c_s t) - 1}{|q| c_s t} \right. \\
 & \left. - \frac{2}{\pi} \int_1^a \frac{4(1 - y^2) \sqrt{1 - y^2/a^2}}{(y^2 - y_R^2)(y^2 - y_1^2)(y^2 - y_2^2)} y \sin(y |q| c_s t) dy \right\},
 \end{aligned}
 \tag{A.1}$$

$$\begin{aligned}
M_{22}(t; q) = c_s |q| \frac{c_s}{\mu} & \left\{ - \int_0^1 \frac{f(y) - f(y_R)}{y - y_R} y \sin(|q| c_s t) dy \right. \\
& + f(y_R) \left[y_R \sin(|q| c_R t) \int_{(|q| c_s t - |q| c_R t)}^{|q| c_R t} \frac{\cos \theta}{\theta} d\theta \right. \\
& \left. \left. - y_R \cos(|q| c_R t) \int_{-|q| c_R t}^{(|q| c_s t - |q| c_R t)} \frac{\sin \theta}{\theta} d\theta \right] + f(y_R) \frac{\cos(|q| c_s t) - 1}{|q| c_s t} \right. \\
& \left. - \frac{2}{\pi} \int_1^a \frac{(2 - y^2)^2 \sqrt{1 - y^2/a^2}}{(y^2 - y_R^2)(y^2 - y_1^2)(y^2 - y_2^2)} y \sin(y |q| c_s t) dy \right\},
\end{aligned} \tag{A.2}$$

$$\begin{aligned}
M_{12}(t; q) &= -i q c_s \frac{c_s}{\mu} \left\{ - \frac{2}{\pi} \int_1^a \frac{2y \sqrt{y^2 - 1} \sqrt{1 - y^2/a^2} (2 - y^2)}{(y_R^2 - y^2)(y_1^2 - y^2)(y_2^2 - y^2)} \cos(y |q| c_s t) dy \right. \\
& \left. + \left(\frac{[-8y_R^2/a^2 + 8/a^2 - y_R^4 - 4 + 6y_R^2 + 2\sqrt{1 - y_R^2} \sqrt{1 - y_R^2/a^2} (2 - y_R^2)]}{(y_1^2 - y_R^2)(y_2^2 - y_R^2)} \right) \cos(|q| c_R t) \right\},
\end{aligned} \tag{A.3}$$

$$M_{33}(t; q) = c_s |q| \frac{c_s}{\mu} J_1(|q| c_s t), \tag{A.4}$$

with

$$\begin{aligned}
g(y) &= \frac{2}{\pi} \frac{4(1 - y^2) \sqrt{1 - y^2/a^2} + (2 - y^2)^2 \sqrt{1 - y^2}}{(y + y_R)(y^2 - y_1^2)(y^2 - y_2^2)} \\
f(y) &= \frac{2}{\pi} \frac{4(1 - y^2/a^2) \sqrt{1 - y^2} + (2 - y^2)^2 \sqrt{1 - y^2/a^2}}{(y + y_R)(y^2 - y_1^2)(y^2 - y_2^2)},
\end{aligned}$$

where $s = p/|q|c_s$, $a = c_d/c_s$ and $y_R = c_R/c_s$. c_R is the Rayleigh wave speed.

References

1. Vanossi, A., Dietzel, D., Schirmeisen, A., Meyer, E., Pawlak, R., Glatzel, T., Kisiel, M., Kawai, S., Manini, N., Recent highlights in nanoscale and mesoscale friction, *Beilstein J. Nanotechnol.* 9 (2018) 1995–2014.
2. Tian, K., Goldsby, D. L., Carpick, R. W., Rate and state friction relation for nanoscale contacts: thermally activated Prandtl-Tomlinson Model with chemical aging, *Phys. Rev. Lett.* 120 (2018) 186101.
3. Zhang D., Li Z., Klausen L.H., Li Q., Dong M.D., Friction behaviors of two-dimensional materials at the nanoscale, *Mater. Today Phys.* 27 (2022) 100771.
4. Weber, B., Scheibert, J., de Boer, M. P., Dhinojwala, A., Experimental insights into adhesion and friction between nominally dry rough surfaces, *MRS Bulletin* 47 (2022) 1237–1246.
5. Vakis, A. I., Yastrebov, V. A., Scheibert, J., Nicola, L., Dini, D., Minfray, C., Almqvist, A., Paggi, M., Lee, S., Limbert, G., Molinari, J. F., Anciaux, G., Echeverri Restrepo, S., Papangelo, A., Cammarata, A., Nicolini, P., Aghababaei, R., Putignano, C., Stupkiewicz, S., Lengiewicz, J., Costagliola, G., Bosia, F., Guarino, R., Pugno, N.M., Müser, M.H., Modeling and simulation in tribology across scales: An overview, *Tribol. Int.* 125 (2018) 169–199.
6. Gustafsson A, Isaksson H., Phase field models of interface failure for bone application - evaluation of open-source implementations, *Theor. Appl. Fract. Mech.* 121 (2022) 103432.
7. Quoc Bui, T., Hu, X., A review of phase-field models, fundamentals and their applications to composite laminates, *Eng. Fract. Mech.* 248 (2021) 107705.

8. Reches, Z., Fineberg, J., Earthquakes as dynamic fracture phenomena, *J. Geophys. Res.* 128 (3) (2023) e2022JB026295.
9. Weng, H., Ampuero, J.P., Integrated rupture mechanics for slow slip events and earthquakes, *Nat. Commun.* 13 (1) (2022) 7327.
10. Harris, R.A., Archuleta, R.J., Earthquake Rupture Dynamics: Comparing the Numerical Simulation Methods, *EOS* (85) (34) (2004) 321.
11. Roch, T., Barras, F., Geubelle, P.H., Molinari, J.F., cRacklet: a spectral boundary integral method library for interfacial rupture simulation, *J. Open Source Software* 17 (2022) 3724.
12. Gvirtsman, S., Fineberg, J., Nucleation fronts ignite the interface rupture that initiates frictional motion, *Nature Physics* 17 (9) (2021) 1037-1042.
13. Shlomai, H., Kammer, D.S., Adda-Bedia, M., Fineberg, J., The onset of the frictional motion of dissimilar materials, *Proceedings of the National Academy of Sciences* 117 (24) (2020) 13379-13385.
14. Adams, G.G., Self-excited oscillations of two elastic half-spaces sliding with a constant coefficient of friction, *J. Appl. Mech.* 62 (1995) 867–872.
15. Achenbach, J.D., Epstein, H.I., Dynamic interaction of a layer and a half-space, *J. Eng. Mech. Div. EM5* (1967) 27–42.
16. Ranjith, K., Rice, J.R., Slip dynamics at an interface between dissimilar materials, *J. Mech. Phys. Solids* 49 (2001) 341–361.
17. Rice, J.R., Lapusta, N., Ranjith, K., Rate and state dependent friction and the stability of sliding between elastically deformable solids, *J. Mech. Phys. Solids* 49 (2001) 1865–1898.
18. Adams, G.G., Steady sliding of two elastic half-spaces with friction reduction due to interface stick-slip, *J. Appl. Mech.* 65 (1998) 470–475.

19. Ranjith, K., Destabilization of long-wavelength Love and Stoneley waves in slow sliding, *Int. J. Solids Struct.* 46 (2009) 3086–3092.
20. Love, A.E.H., *Some problems of geodynamics*, Cambridge University Press, Cambridge (1911).
21. Stoneley, R., Elastic waves at the surface of separation of two solids, *Proc. R. Soc. A* 106 (1924) 416-428.
22. Harris, R. A., Day, S.M., Effects of a low-velocity zone on a dynamic rupture, *Bull. Seismol. Soc. Amer.* 87 (1997) 1267-1280.
23. Andrews, D.J., Ben-Zion, Y., Wrinkle-like slip pulse on a fault between different materials, *J. Geophys. Res.* 102 (1997) 553-571.
24. Langer, S., Olsen-Kettle, L., Weatherley, D., Identification of supershear transition mechanisms due to material contrast at bimaterial faults, *Geophys. J. Int.* 190 (2012) 1169-1180.
25. Kammer, D.S., Yastrebov, V. A., Anciaux, G., Molinari, J.F., The existence of a critical length scale in regularised friction, *J. Mech. Phys. Solids* 63 (2014) 40-50.
26. Kammer, D.S., Yastrebov, V. A., Spijker, P., Molinari, J.F., On the propagation of slip fronts at frictional interfaces, *Tribol. Lett.* 48 (2012) 27–32.
27. Cochard, A., Rice, J.R., Fault rupture between dissimilar materials: Ill-posedness, regularization, and slip-pulse response, *J. Geophys. Res.* 105 (2000) 25891–25907.
28. Ampuero, J.P., Ben-Zion, Y., Cracks, pulses and macroscopic asymmetry of dynamic rupture on a bimaterial interface with velocity-weakening friction, *Geophys. J. Int.* 173 (2008) 674–692.

29. Budiansky, B., Rice, J.R., An integral equation for dynamic elastic response of an isolated 3-D crack, *Wave Motion* 1 (1979) 187–192.
30. Kostrov, B.V., Unsteady propagation of longitudinal shear cracks, *J. Appl. Math. Mech.* 30 (1966) 1241–1248.
31. Geubelle, P.H., Rice, J.R., A spectral method for three-dimensional elastodynamic fracture problems, *J. Mech. Phys. Solids* 43 (1995) 1791–1824.
32. Geubelle, P.H., Breitenfeld, M.S., Numerical analysis of dynamic debonding under anti-plane shear loading, *Int. J. Fract.* 85 (1997) 265–282.
33. Breitenfeld, M.S., Geubelle, P.H., Numerical analysis of dynamic debonding under 2D in-plane loading and 3D loading, *Int. J. Fract.* 93 (1998) 13–38.
34. Ranjith, K., Spectral formulation of the elastodynamic boundary integral equations for bi-material interfaces, *Int. J. Solids Struct.* 59 (2015) 29–36.
35. Ranjith, K., Spectral formulation of the boundary integral equation method for antiplane problems, *Mech. Mater.* 165 (2022) 104177.
36. Cochard, A., Madariaga, R., Dynamic faulting under rate-dependent friction, *Pure Appl. Geophys.* 142 (1994) 419–445.
37. Kausel, E., Lamb’s problem at its simplest, *Proc. R. Soc. A* 469 (2013) 20120462.
38. Harris, R. A., M. Barall, R. Archuleta, E. Dunham, B. Aagaard, J. P. Ampuero, H. Bhat, et al., The SCEC/USGS dynamic earthquake rupture code verification exercise, *Seismo. Res. Lett.* 80 (2009) 119–126.
39. Albertini, G., Elbanna, A., Kammer, D.S., A three-dimensional hybrid finite element-spectral boundary integral method for modeling earthquakes in complex unbounded domains, *Int. J. Numer. Methods Eng.*, 122 (23) (2021) 6905– 6923.

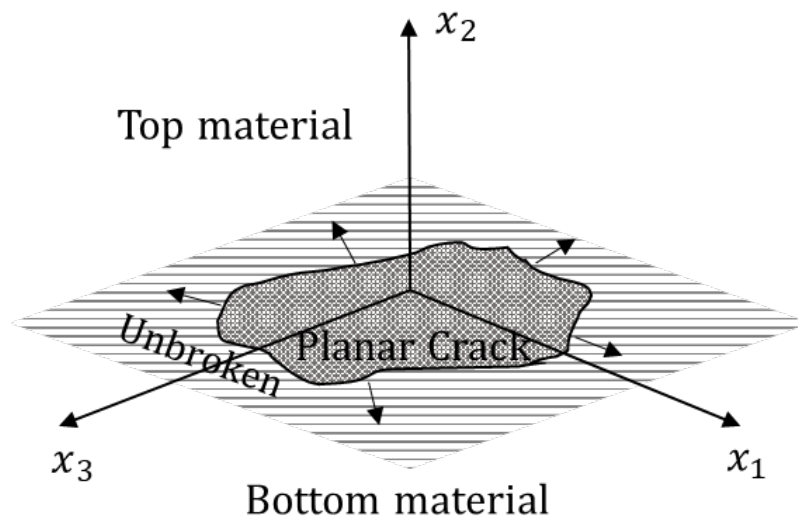


FIGURE 1 Problem geometry for three-dimensional rupture propagation in a plane.

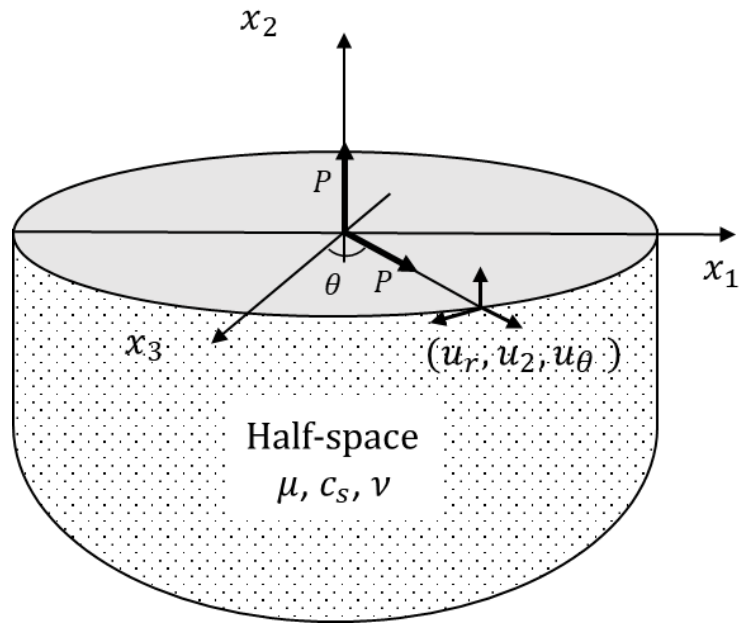


FIGURE 2 Problem geometry of 3D Lamb problem for a half-space.

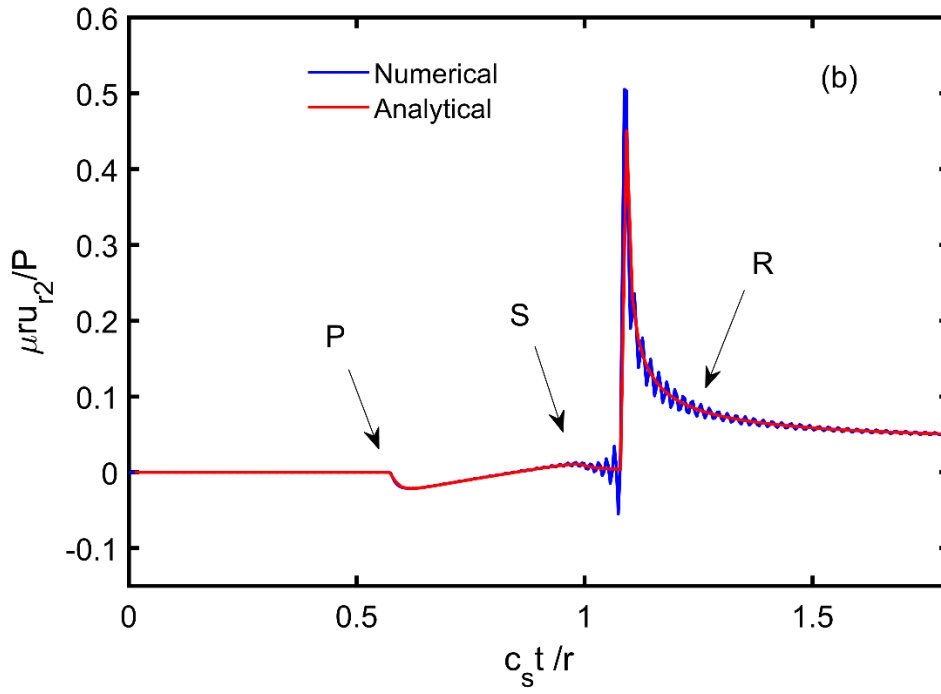
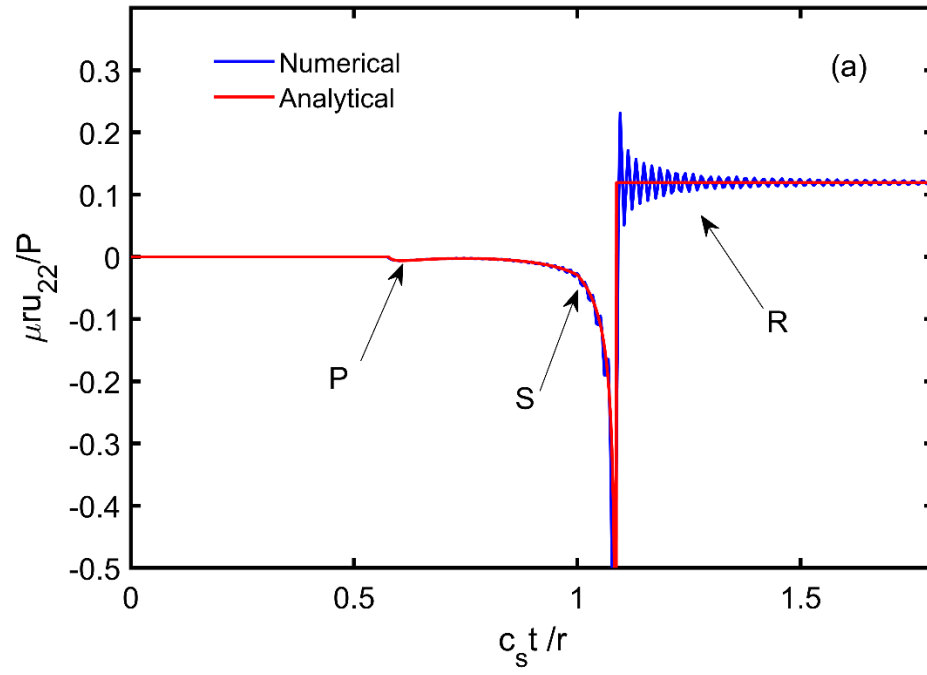


FIGURE 3 (a) Vertical and (b) Radial displacements at a location due to applied normal line load at mid-point of the free surface.

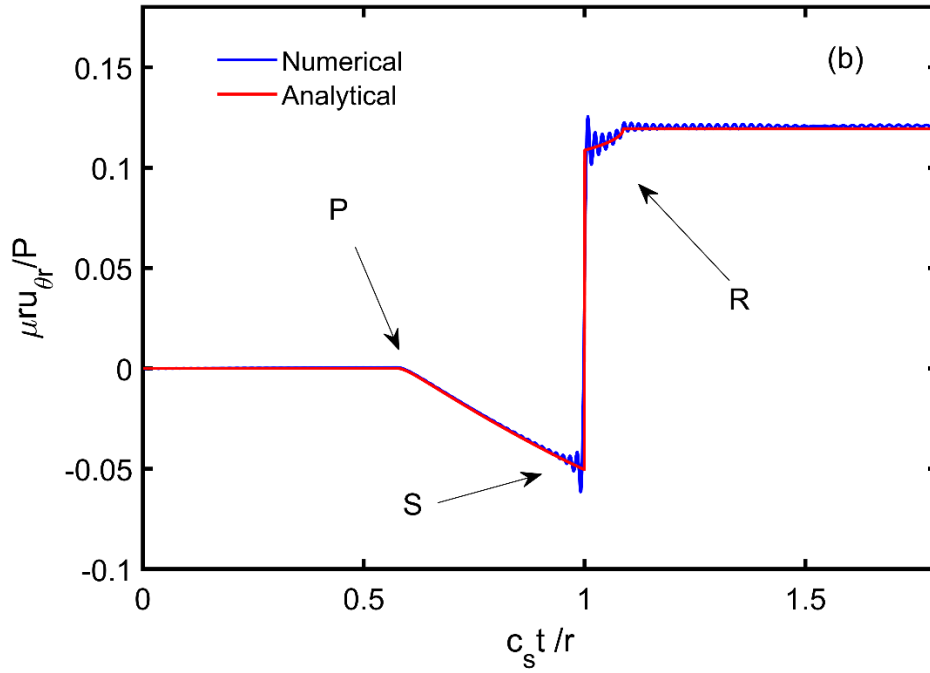
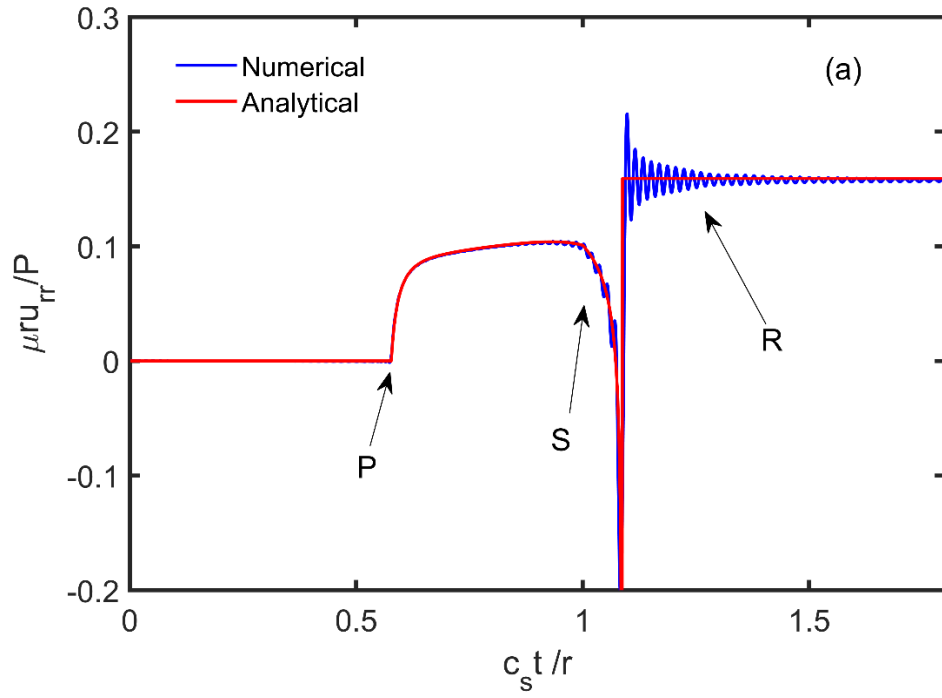


FIGURE 4 (a) Radial and (b) Tangential displacements at a location due to applied horizontal line load at the mid-point of free surface.

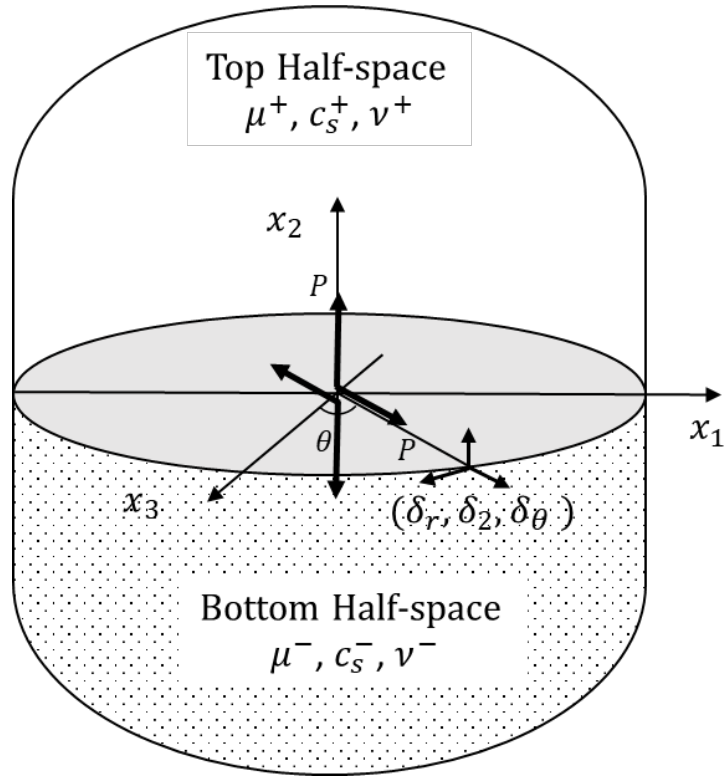


FIGURE 5 Problem geometry of 3D Lamb problem at the interface between two distinct half-spaces.

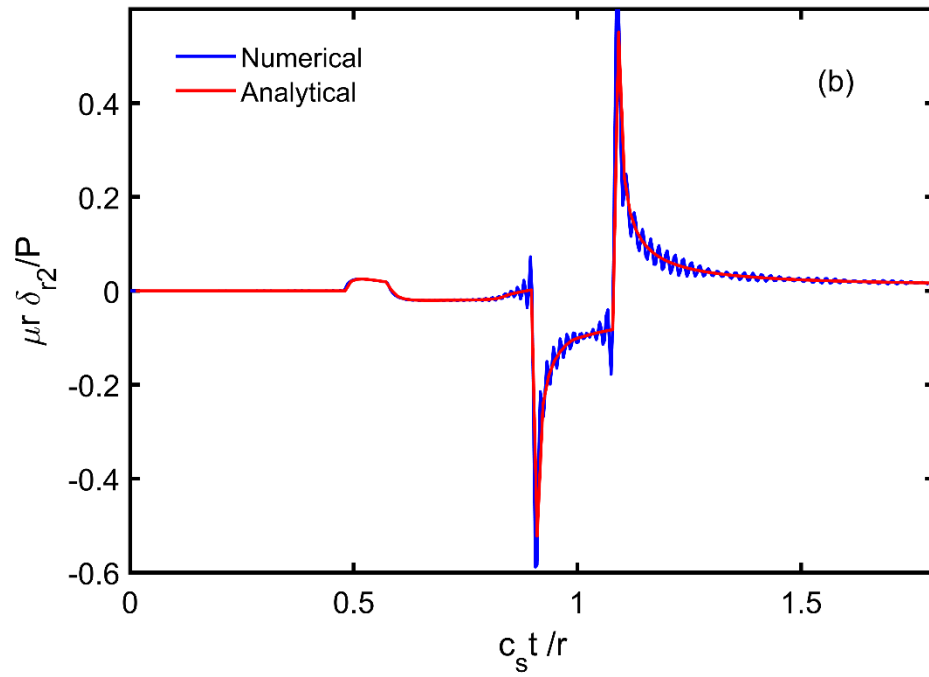
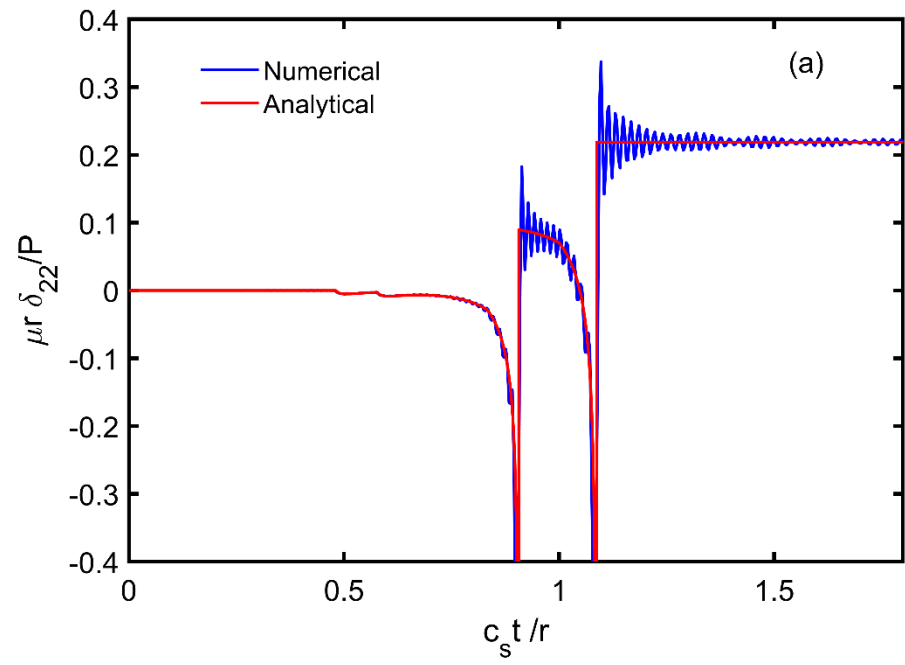


FIGURE 6 (a) Vertical and (b) Radial slips at a location due to applied normal line load at the center of planar interface.

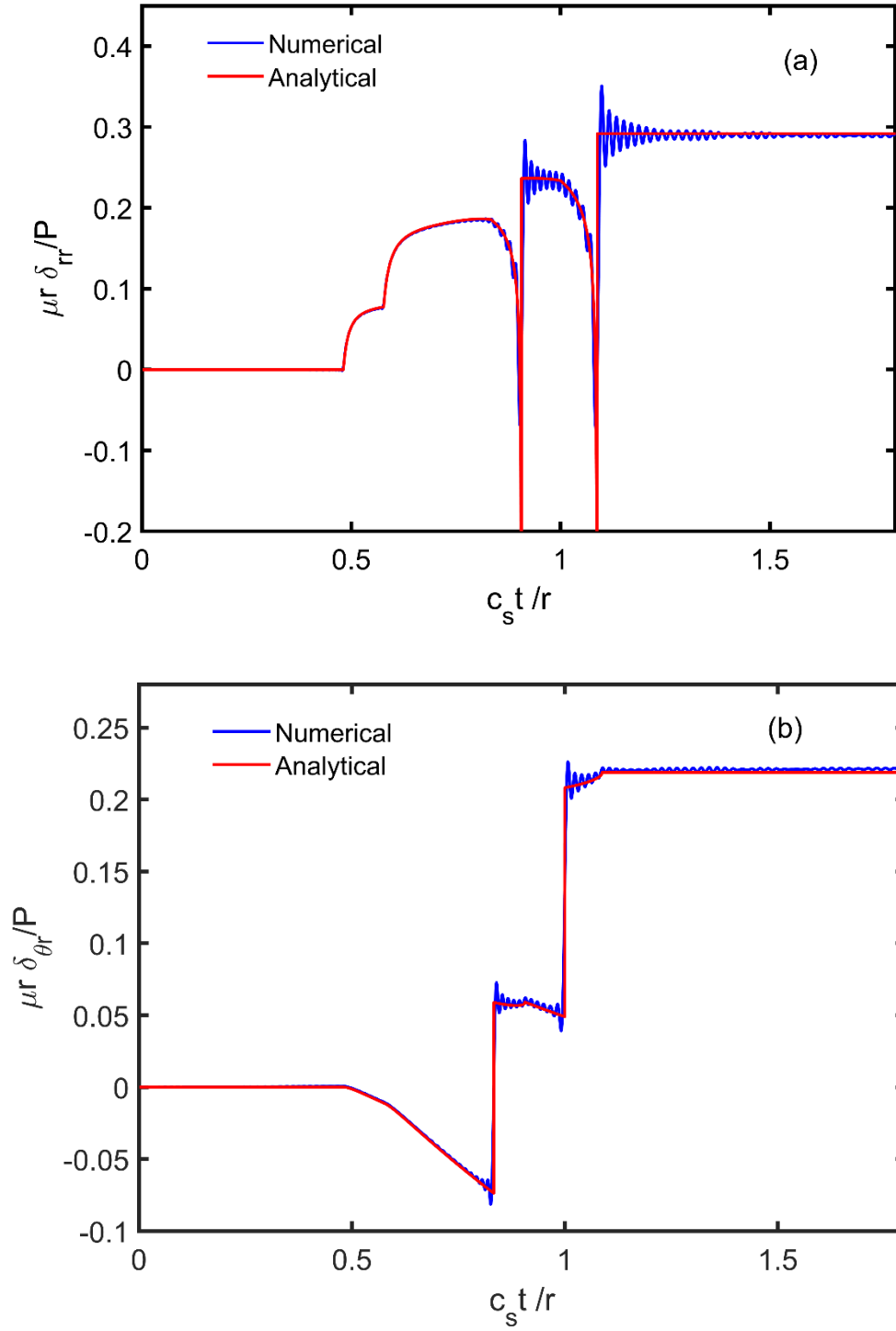


FIGURE 7 (a) Radial and (b) Tangential slips at a location due to applied horizontal line load at the center of planar interface.

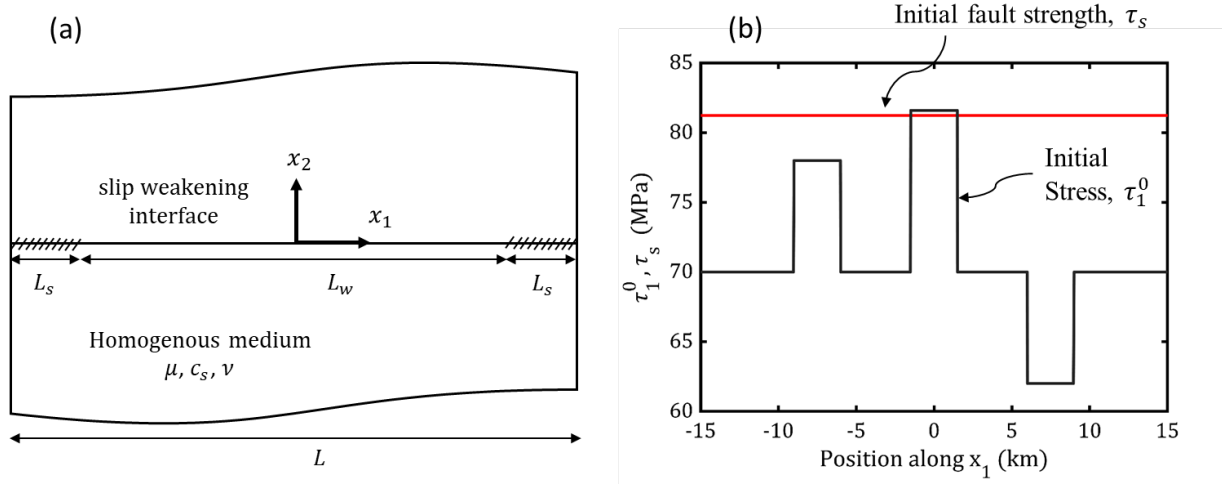


FIGURE 8 The configuration of TPV 205-2D, which involves a fault situated within a uniform medium. Panel (a) describes the problem geometry and panel (b) shows the initial stress distribution and frictional strength along the interface.

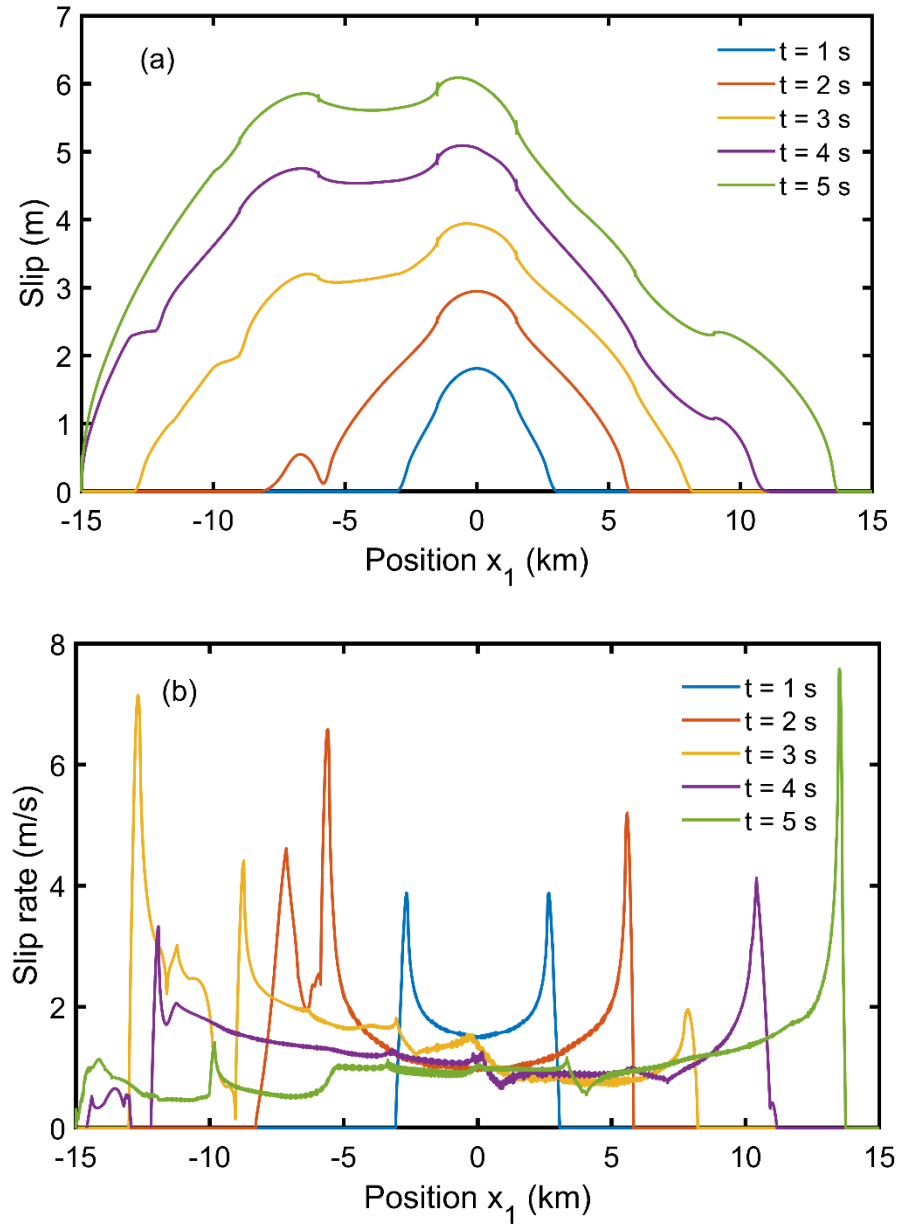


FIGURE 9 Snapshots of (a) slip and (b) slip rate along the interface for TPV 205-2D benchmark problem at $t = 1$ s, 2 s, 3 s, 4 s, 5 s.

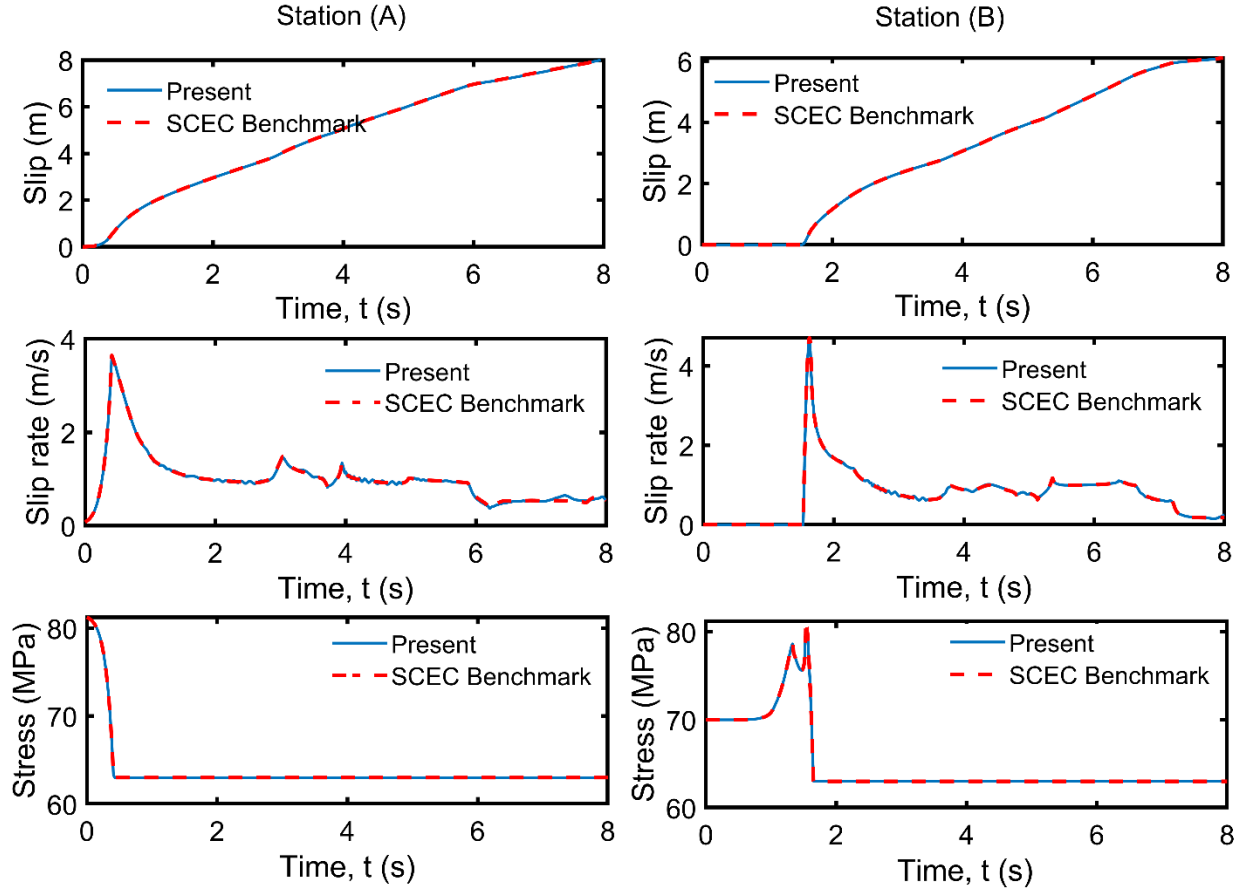


FIGURE 10 Temporal evolution of the slip, slip rate, and shear traction at two stations: (A) in the center of the fault and at a station (B) 4.5 km away from the center of the fault for TPV 205-2D problem. 8192 elements are used in the present simulation.

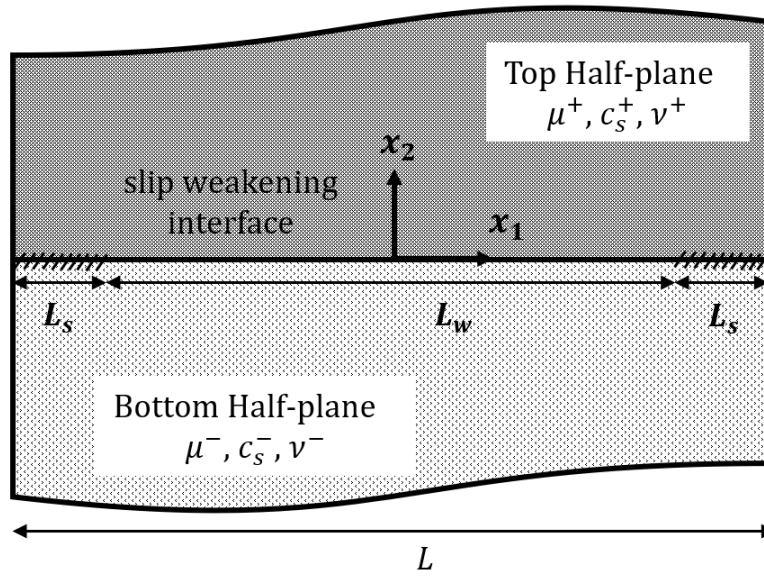


FIGURE 11 Problem geometry for 2D dynamic rupture along a bi-material interface.

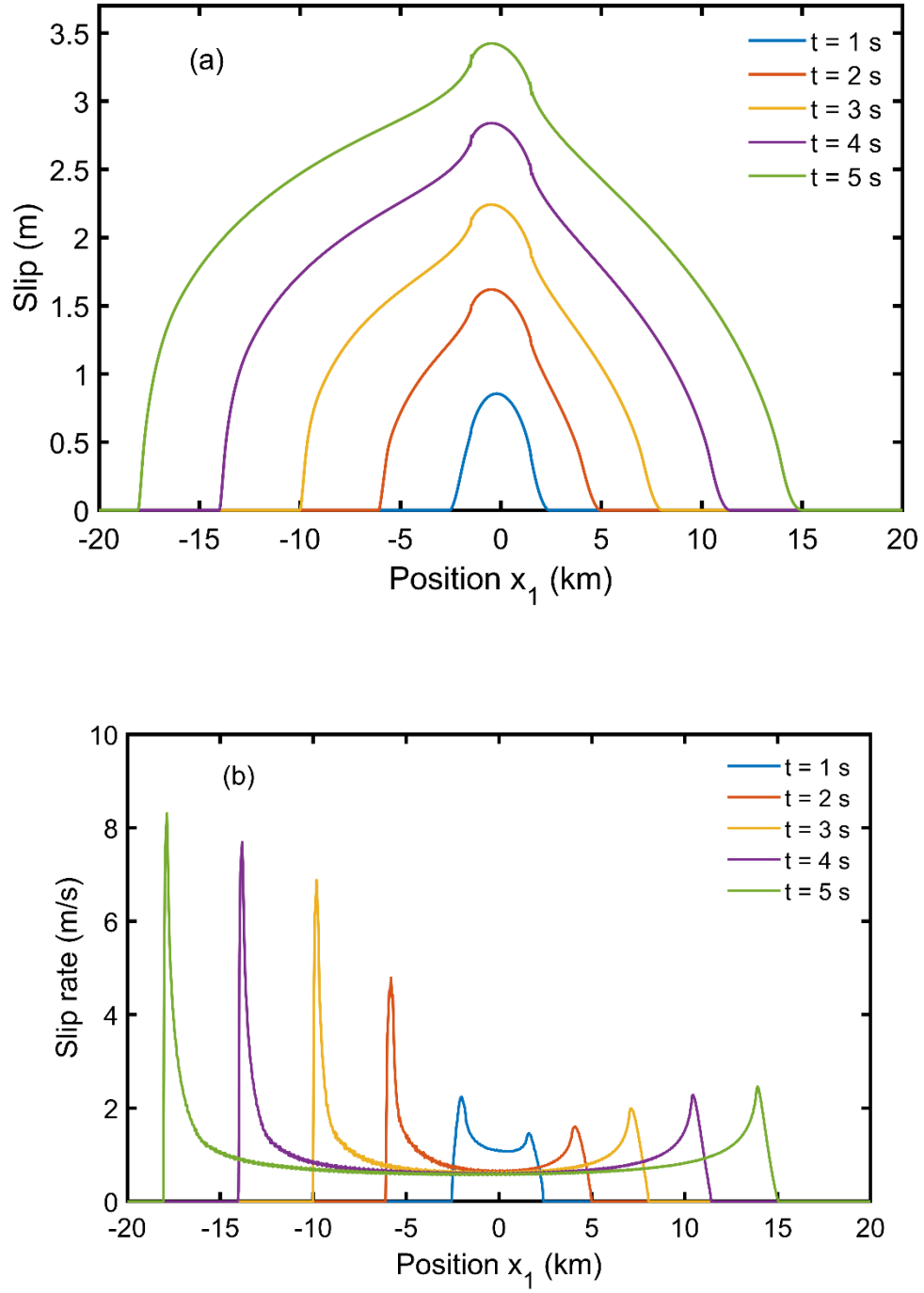


FIGURE 12 Snapshots of (a) slip and (b) slip rate along the interface at $t = 1$ s, 2 s, 3 s, 4 s, 5 s for elastic mismatch parameters characterized as $c_s^-/c_s^+ = 2$ and $\rho^-/\rho^+ = 1.2$ (well-posed problem). 2048 elements are used in this simulation.

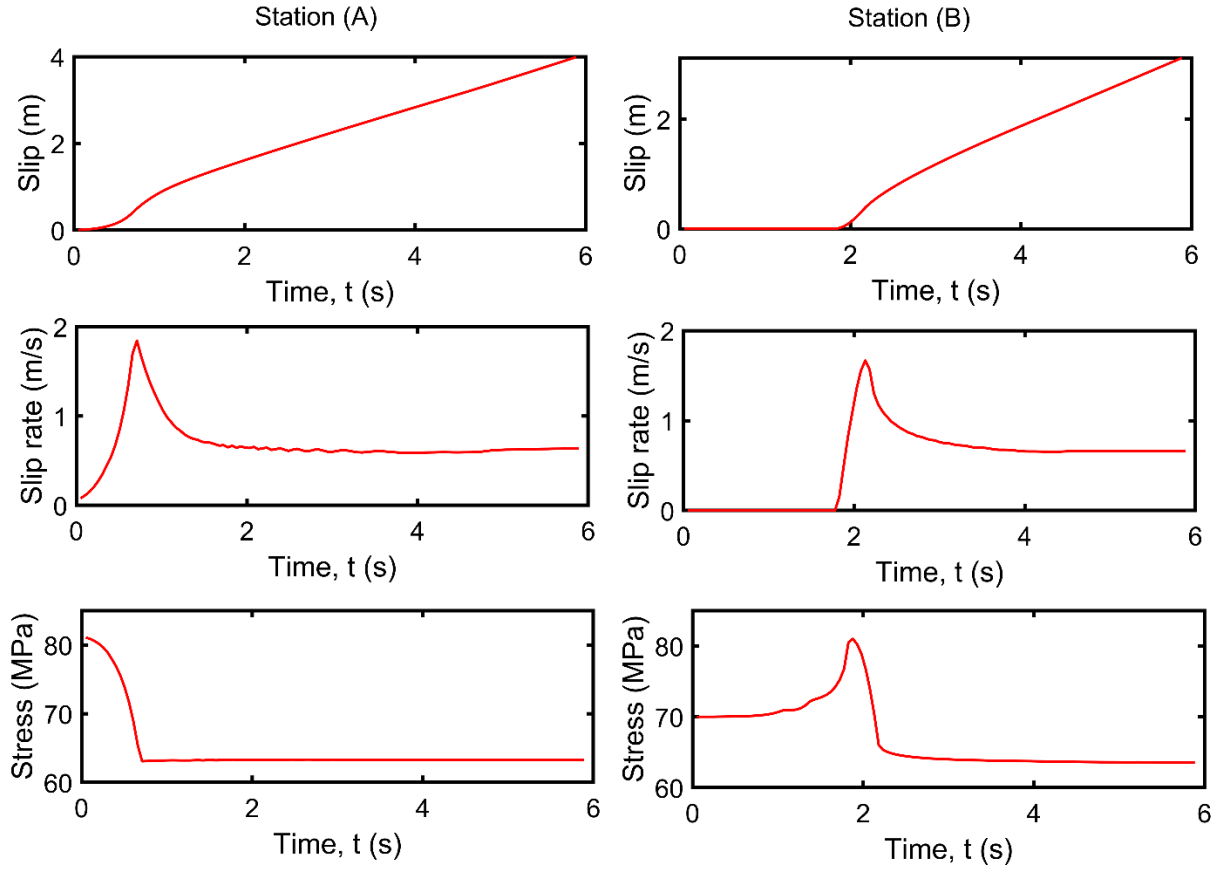


FIGURE 13 Temporal evolution of the slip, slip rate, and shear stress at two stations: (A) in the center of the fault and at a station (B) 4.5 km away from the center of the fault for well-posed problem. 2048 elements are used in this simulation.

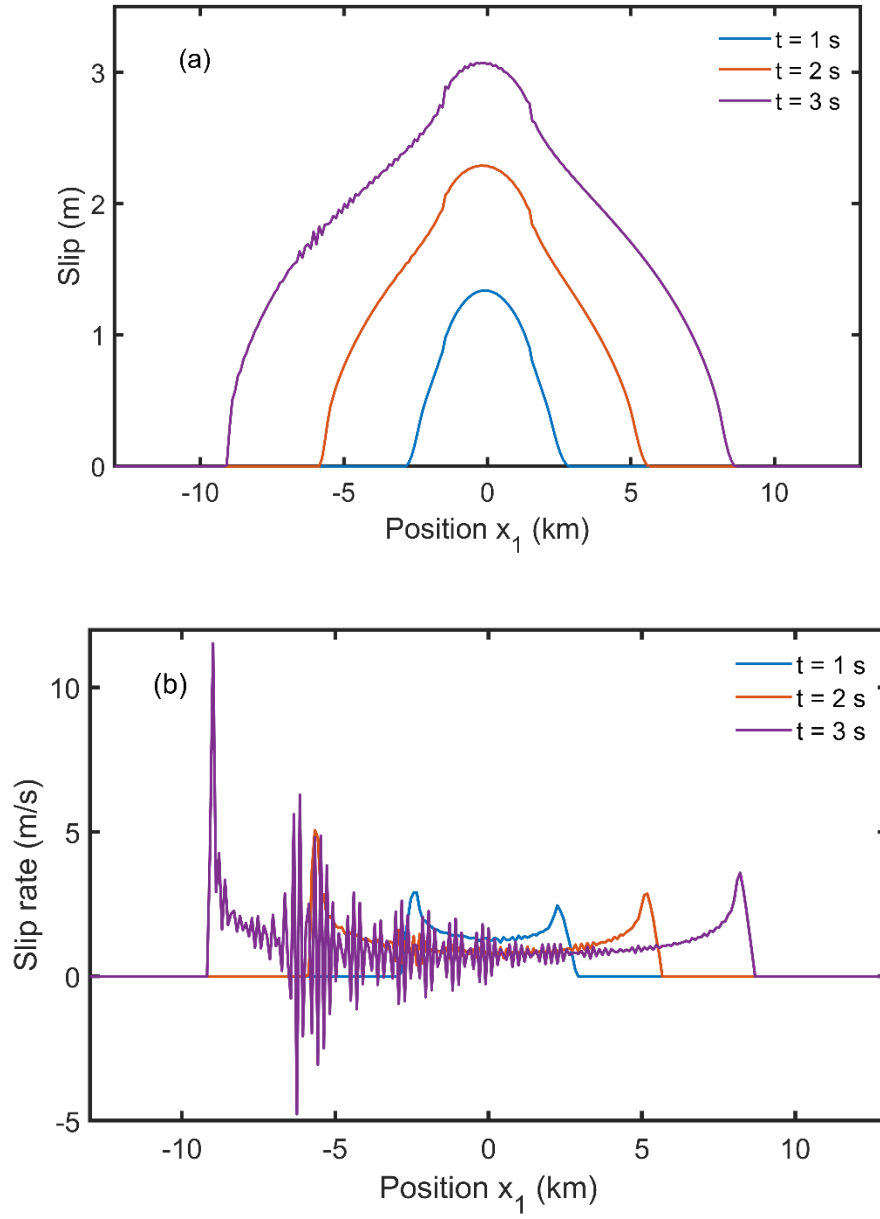


FIGURE 14 Snapshots of (a) slip and (b) slip rate along the interface at $t = 1$ s, 2 s, 3 s for elastic mismatch parameters characterized as $c_s^-/c_s^+ = 1.2$ and $\rho^-/\rho^+ = 1.2$ (ill-posed problem). 2048 elements are used in this simulation.

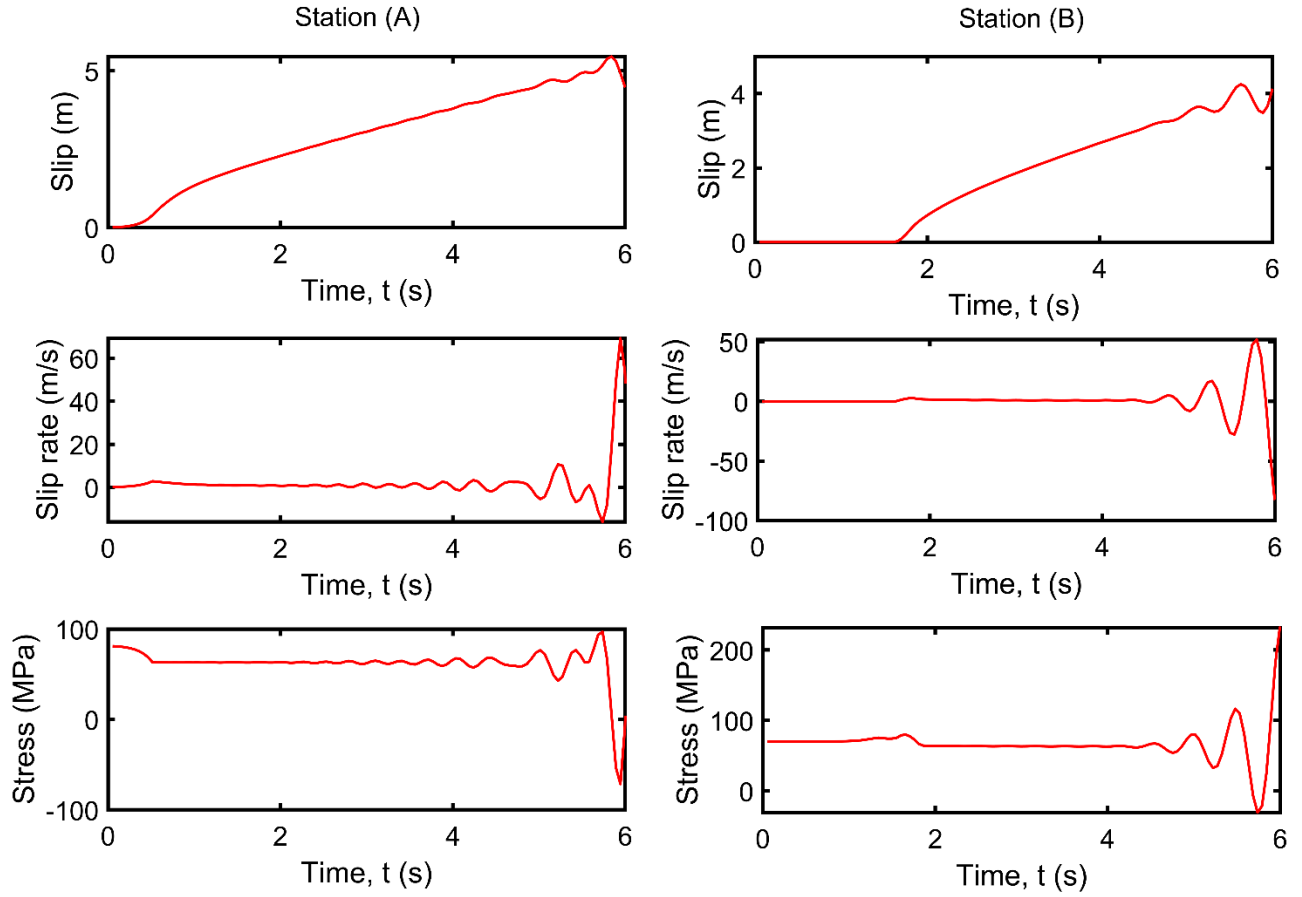


FIGURE 15 Temporal evolution of the slip, slip rate, and shear stress at two stations: (A) in the center of the fault and at a station (B) 4.5 km away from the center of the fault. 2048 elements are used in this simulation.

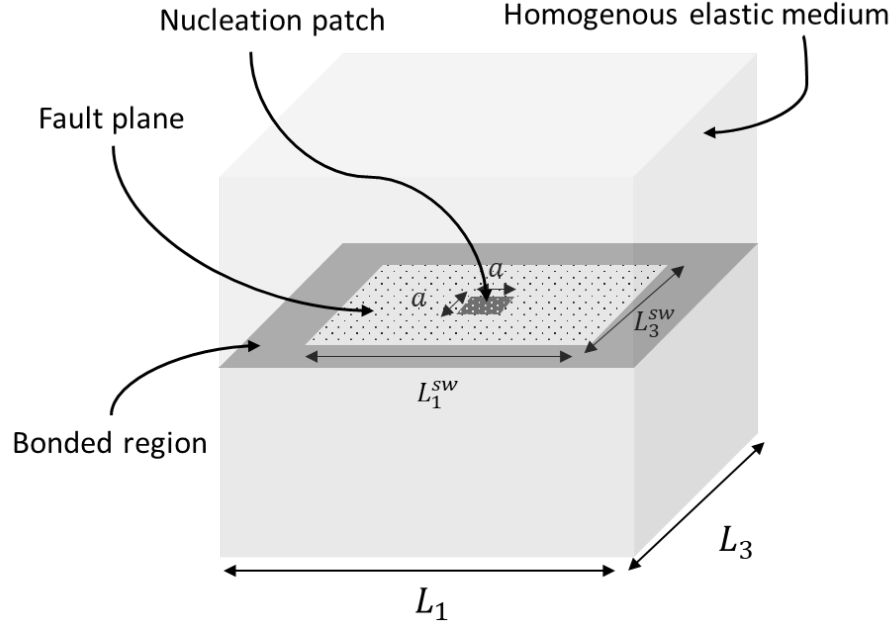


FIGURE 16 Problem geometry of TPV3 benchmark problem for 3D rupture propagation in a homogeneous medium.

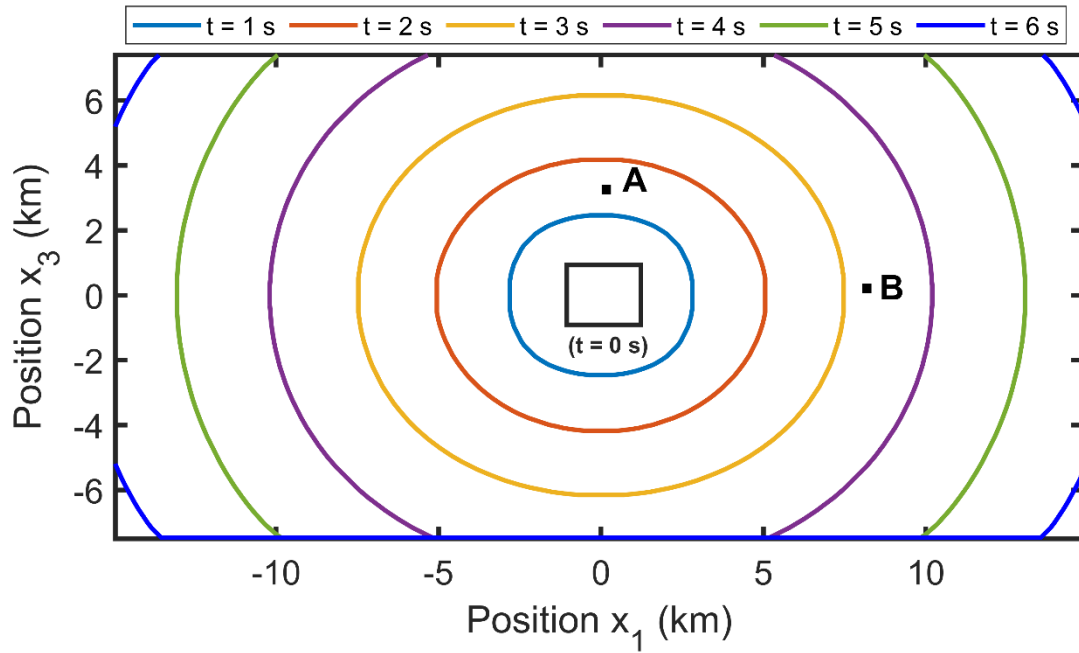


FIGURE 17 Evolution of rupture font position with time, $t = 0$ s to 6 s in TPV3 problem. 1024*512 square grid elements are used in this simulation.

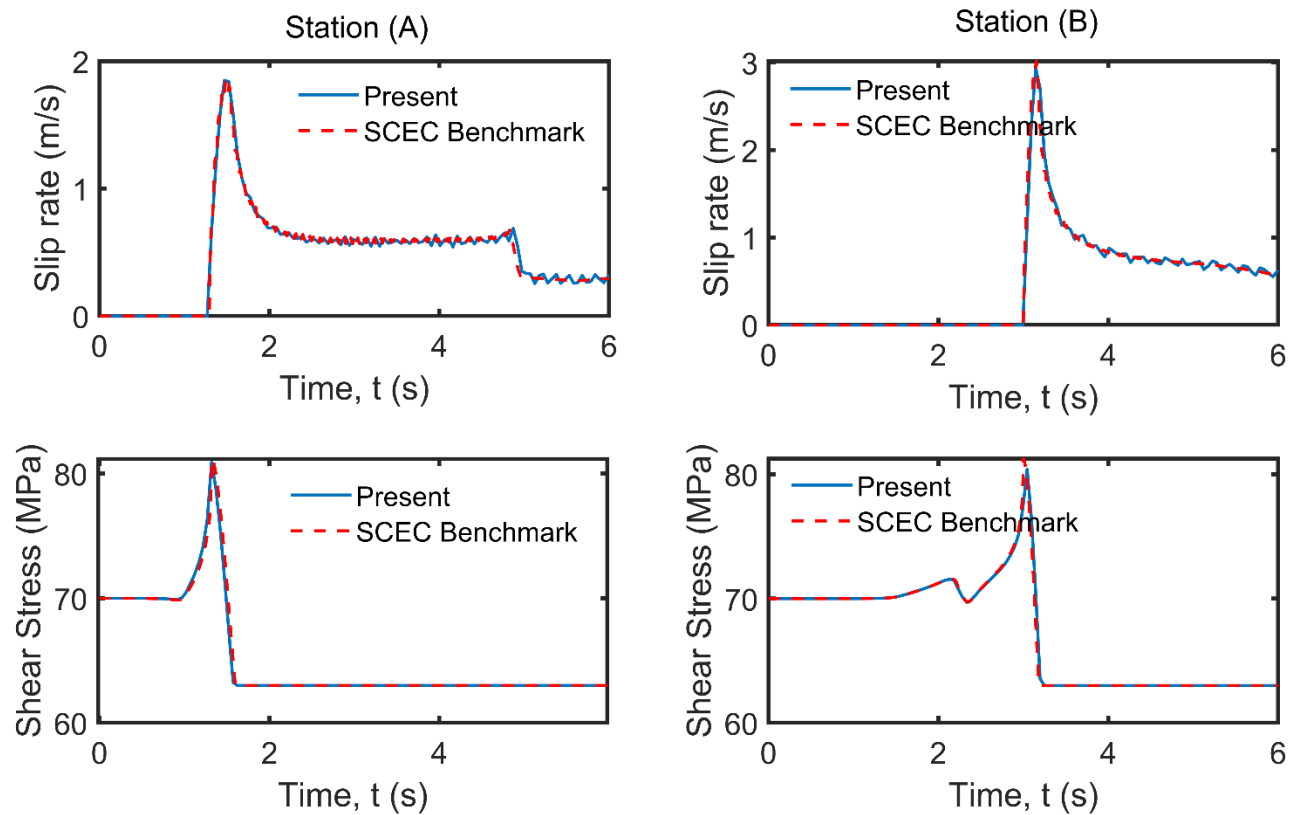


FIGURE 18 Temporal evolution of the fault slip rate and shear stress at two stations A and B in TPV3 problem. 1024*512 square grid elements are used in this simulation.

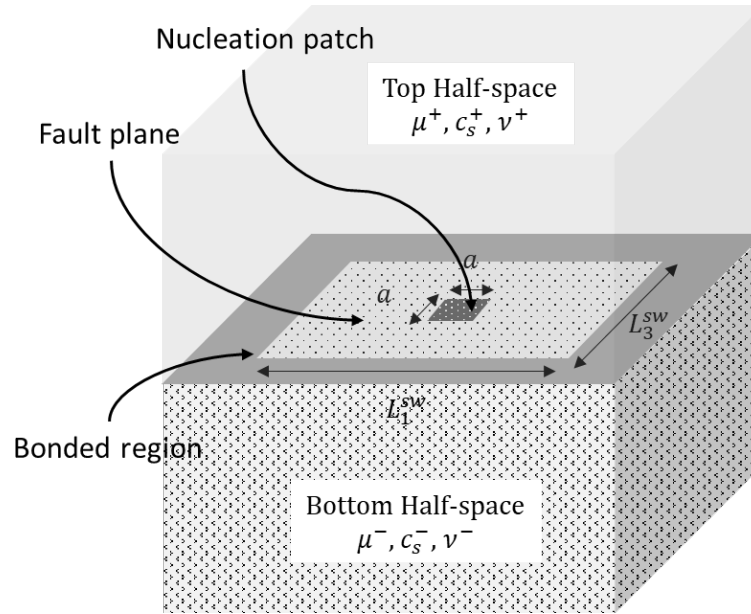


FIGURE 19 Problem geometry for a fault between two elastic half-space having dissimilar elastic properties.

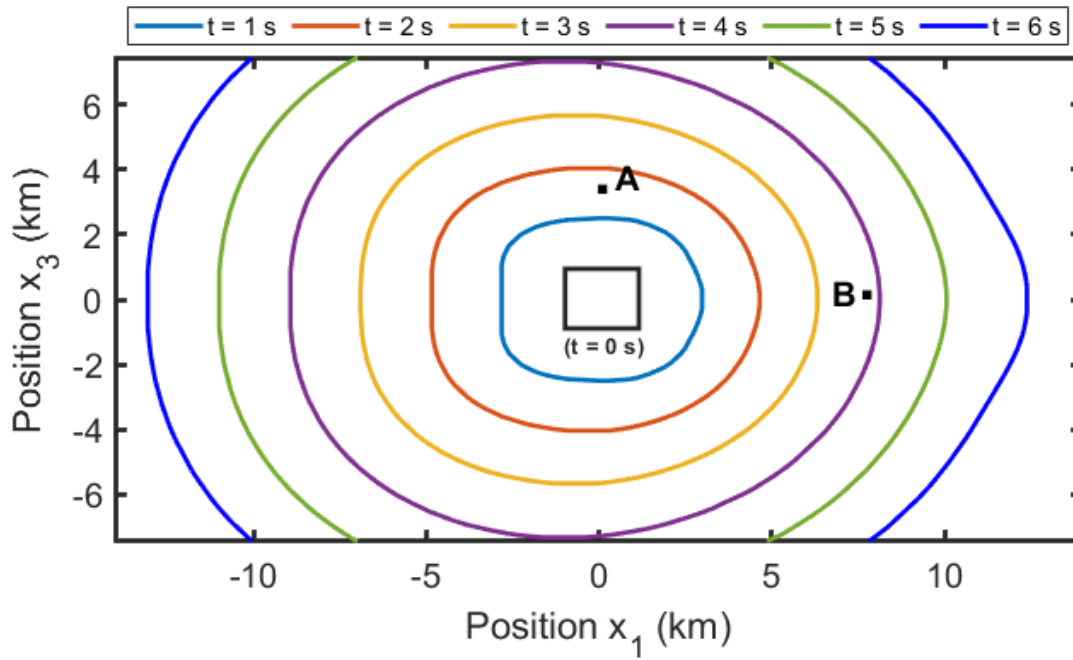


FIGURE 20 Evolution of rupture front position with time, $t = 0 \text{ s}$ to 6 s for a bi-material interface. 1024*512 square grid elements are used in this simulation.

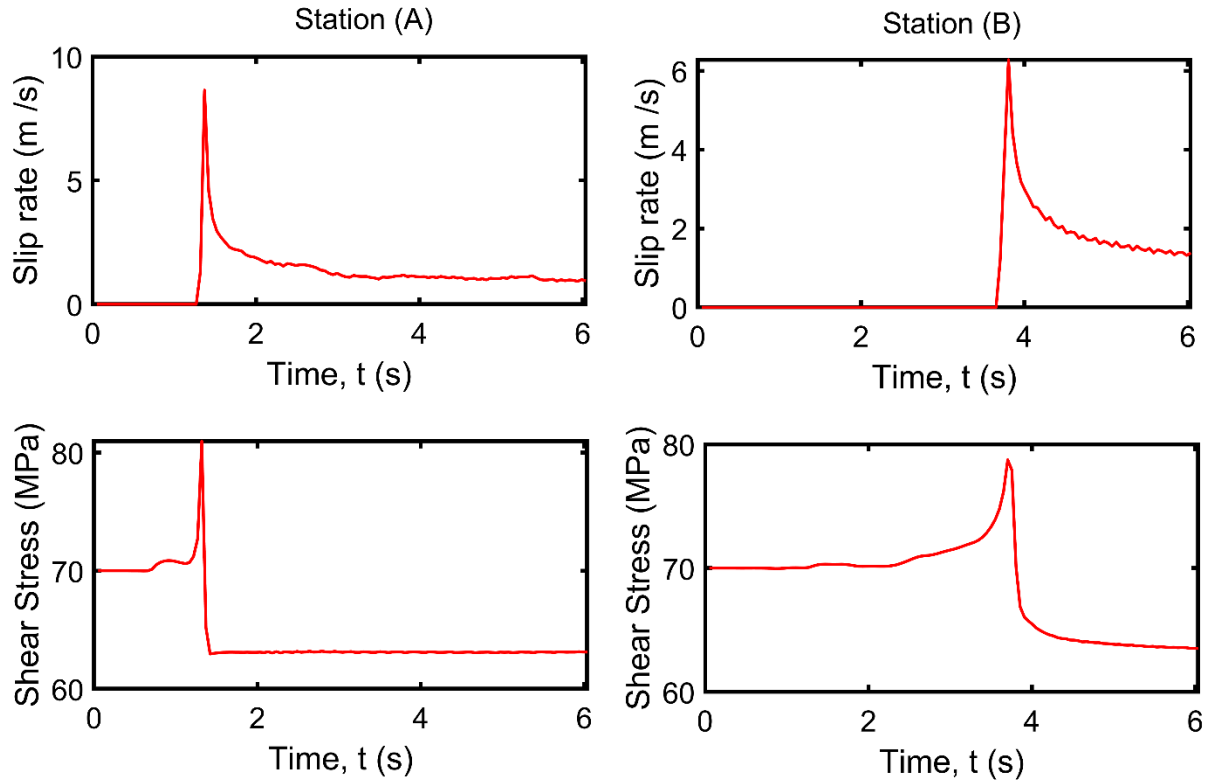


FIGURE 21 Temporal evolution of the fault slip rate and shear stress at two stations A and B along a bi-material interface. The material parameters are chosen so that the problem is well-posed. 1024*512 square grid elements are used in this simulation.